TFM-250MMNE12-COMPUTATIONAL ANALYSIS OF THE REMODELING IN BIOLOGICAL TISSUE

Mauricio Barrera Cárdenas

September 27, 2022

Contents

1

Summary

This work documents an implementation of a fibre reorientation model, or remodelling formulation, on the basis of a fibre-reinforced hyperelastic material. Furthermore, two models are considered to represent the mechanical deformation of the fibres themselves: exponential and Worm-Like Chain (WLC). The fibre behaviour was carried along to a macro-scale response by the microsphere approach for multiscale modelling. The fibres are embedded in a ground substance represented by a NeoHookean isotropic strain energy function.

In addition to the fibre reorientation at a single point, we also studied how this reorientation propagates in space as one moves away from a boundary of prescribed displacement, where the whole process is initiated. It is hypothesised that the anisotropy gain implied by remodelling confers stiffness to the material, and so its propagation in space leads to increased stresses in the direction of prescribed displacement.

The geometry used to study the implemented model consists of a plate with two holes; they represent two neighbouring contractile cells, whereby the space in between them was sampled to see the evolution of stress components and of an anisotropy evolution parameter.

This scenario is of relevance in, for instance, the study of the Long Range Force Transmission (LRFT) phenomenon, which attempts explaining the observed cell alignment and matrix stiffening in connective tissues. LFRT is associated to cell patterning during development of muscle and tendons, but also to life threatening conditions such as cancer propagation, pulmonary fibrosis and liver cirrhosis. One initiator of the LFRT phenomenon is the contractile deformation of cells like fibroblasts; this prescribed deformation simultaneously elicits reorientation of collagen fibres, thus rendering the extracellular matrix anisotropic.

Keywords: Collagen fibre remodelling, connective tissue mechanics, microspheres and remodelling, hyperelasticity and internal variables.

2

Introduction

2.1 Mechanics of Fibre-Reinforced Soft Tissues

2.1.1 General Aspects

The formulation of mathematical models to study the mechanical behaviour of fibre-reinforced soft biological tissues takes place mostly in the frame of continuum mechanics of hyperelastic, anisotropic materials. It allows a separate formulation of strain energies for the volumetric deformation, the isotropic ground substance and the anisotropic contribution from a set of fibre families. Once here, however, there has been a series of approaches, mainly marked by capturing the mechanical behaviour of the reinforcing collagen fibres at the molecular lever, and then conveying these micro-models to a macroscopic-level response [15]. Some call this process mathematical homogenisation [35], and it encompasses a wide variety of modelling approaches to multi-scale phenomena.

Although hyperelastic models are usually assumed to be incompressible, the observed response of anisotropic tissue to hydrostatic loading motivated the formulation of models in which the strain energy contribution from the fibre phase depends on the whole set of stress invariants [53]; this forces to consider explicitly a volumetric strain energy. By the same argument, other study proposes a model whereby the isotropic matrix is poro-viscoeleastic, while the fibre contribution remains dependent on the isochoric part of deformation tensors only [40]. In this case, the claim is that such approach appropriately models the response of tendons and cartilage present in large joints, in a similar way to how porous materials -soil for instance- interact with fluids that can seep through their volume [19].

While there are two main fibrous components relevant to the behaviour of connective tissue, elastin and collagen, the latter makes up the most fraction and behaves as load carrying member [5]. Elastin is less stiff than collagen, and contributes to the spring-back reaction of tissue to external stretching. It is regarded as an intrinsic component of the isotropic extracellular matrix, and therefore in

charge of determining its elastic properties [14]. It is usual modelling it using the Neo-Hookean strain energy function.

Accounting for fibre contribution to strain energy in terms of invariants of the isochoric part of stress and deformation tensors is usual, but it is not the only approach applied to acceptable models. One such case considers the stress as a linear combination of nth-order derivatives of the strain energy, each multiplied by deformation invariants of the corresponding same degree [32]; this makes dispersion measures be easily incorporated, and their effects are thus deemed as special cases of the proposed framework.

2.1.2 Microspheres, fibre properties and remodelling

One important aspect of modelling the mechanical response of the tissue is that of linking the models at the microscopic, molecular level of the fibre constituents to the macroscopic response. The microscopic-scale models can be either 1D representations of molecules or geometrically simple assemblies thereof; macroscopic response is a continuum mechanics description of matter in 3D space, at a much larger size scale. One strategy is the so-called microsphere approach, whereby a 1D model of the mechanics at molecular level is but a member or fibre of a set that follows some given statistical orientation distribution function (ODF) [2]; this ODF is, in turn, a key component of some modelling efforts of fibre dispersion about a preferred direction [31]. The set of accordingly dispersed fibres is then averaged by integration over a unit sphere using an quadrature-like method; the choice of discrete directions and their weights can significantly influence the accuracy of the predictions made with such models [2, 51]. Furthermore, the mechanical contribution of a fibre to the 3D nature of the continuum is obtained by postulating that the strain energy function ψ is even with respect to a vector $\mathbf{r}_i$ associated to each fibre [29]. Hence, this dependency can be set forth in the form $\psi(...\mathbf{r}_i \otimes \mathbf{r}_i)$; this dyadic product approach has been used in modelling works, and referred to as structural tensor; for instance, in the context of fibre dispersion effect on the behaviour of arterial layers [23].

As regards modelling the behaviour of individual fibres, there are two mainstream approaches: phenomenological and microstructural. The former follows a simplified, exponential-like description of observed load-deflection tests in a variety of biological tissue samples [22]. It can take many forms given by the choice of several empirical constants, what nonetheless makes it difficult ascribing a precise physical interpretation [34]. Meanwhile, an inverse tangent function, which may resemble an exponential evolution for certain parameter values, has been shown to explain a high percentage of variability in a statistical study of mechanical behaviour of thoracic and abdominal aortas [43]. Recently, attention has been drawn to the fact that anisotropy models that use exponential-like strain energy functions for fibres can lead to prediction of unphysical deformations, such as transverse ex-

pansion in uniaxial tensile tests [20].

As for the microstructure-based models of fibre behaviour, one seminal work is the modelling of the macromolecular network of rubber compounds as an eight-chain model, whereby individual polymer chains are symmetrically laid out in a paralellepiped [4]. This model makes a direct relationship between its micro- and macroscopic measures of stretch, a fact that establishes a further relevant categorisation: affine and non-affine deformation models. Is already recognised that the latter reproduces observed macroscopic deformations with more precision, particularly in non-uniform deformation conditions [42]. The contributions to strain energy from the molecular features of the collagen fibres can be derived from statistical mechanics principles, whereby a probability distribution of certain proposed configurations is enforced [37]. The eight-chain model is generic in the sense that it admits the formulation of special cases, such as orthotropic, 1D scenarios [2, 50]. In addition, this model has also gained popularity thanks to the several standard approaches from statistical mechanics and probabilistic theory that can be applied to the representation of molecules, and the possibility to turn to a variety of dimensional-scaling arguments to convey continuum models of matter [48].

The remodelling of fibre reorientation can turn to the evolution of parameters of the ODF or to the explicit evolution of the orientation of the fibres themselves, as done in this work (i.e. ODF $\rho = 1$). Moreover, in the context of the microsphere approach to modelling, there is a direct association between the direction of the fibres and those of the unit vector used for quadrature integration over the unit sphere [50]. In some formulations, the evolution is driven by some measure of the deformation, an approach which can also be applied to the combination of fibre reorientation and tissue growth [49]. Other models rotate a structural tensor by using a thermodynamics-defined driving force [39], thanks to the fact that the evolution of internal variables in hyperelastic models is associated to a dissipation of energy which can be tracked during calculations [29]. When deformation drives the reorientation of fibres, the difference between the principal stretches of a deformation measure and those from a structural tensor defined in terms of a set of fibres is the main factor that defines the direction of remodelling and the rate at which it happens [27]. Time integration scheme and consistent linearisation to obtain the tangent moduli are the main features of producing a specific formulation.

Yet another way to account for the role of fibre orientation on the stiffening of the material on a preferred direction is proposed by Wang et al. [74]. Here they formulate a continuum, not-multiscale model of fibrous tissue whereby a discrete network of fibres is explicitly discretised, and the orientation of each is made part of the element information. Then, if that direction matches one of the principal axes of stress -within some tolerance-, then the material is automatically endowed a larger stiffness along that direction. The model seems designed to purportedly mimic the force transmission phenomenon.

A common factor to any effort at modelling the mechanics of fibrous biological tissues is that they are constrained by the numerous tissue morphologies present in the body, and to the possibility of measuring their orientation accurately. For instance, in certain zones of the brain, the orientation of axons determine a preferred orientation of localised sets of reinforcing fibres [24], whereby careful establishment of initial anisotropy and quantification of fibre dispersion parameters are crucial to obtain dependable model results. Other model considers only one parameter for the fibre orientation as part of a crack-propagation problem that represents the tearing of an aorta sample [75]; energy release is then used as an output calculation that traces the evolution of tissue tearing, whereas the ground substance is shown to counteract as a tearing-arrest agent. A mechanical model of the aorta section considers one of its layers with an explicit representation of a dispersion parameter for the reinforcing fibres [23]; these also contribute to a pre-stressed state observed when longitudinally cutting open a tubular specimen [68].

2.2   Fibre Orientation and Tissue Behaviour

As already mentioned, the information on fibre orientation in a tissue sample is important in any attempt at modelling; but experimental challenges associated to its measurement pose restrictions to the phenomena that models should address. For instance, there are questions about defining a relevant fibre-length scale in relation to the phenomena to be modelled and to the image analysis tools available [65]. Also, specialised approaches to image processing aimed at producing quantitative data about fibre orientation can also be required [38]. Then again, some studies on mathematical modelling of fibre reinforced ground substance use a uniform distribution of fibre orientations for their analysis [2]. In any case, the general phenomenon accepted for any modelling approach in the case of fibre reinforced soft tissues is that collagen fibres are the main load-carrying members [77]; their individual properties and alignment determine the mechanical properties that mediate load-deformation behaviour and mechanical failure.

Fibre orientation, however, is not a condition that is given at the start of any biological process and remains static, but one that can change due to mechanical stimulation; moreover, mechanical stimulus triggers a feedback scenario whereby force transmission in between cells activates intracellular mechanisms that, in turn, promote changes in their extracellular environment; these changes themselves effect, finally, fibre reorientation [25]. In connective tissues in between muscular fibres, originally crimpled bundles of collagen fibrils get aligned by the strain induced by stretching sarcomeres [57]. Also, stress concentrators force the alignment of fibres, as tested in a notched section of porcine, aortic sample [59]. Then again, fibre reorientation and stiffening, though experimentally evident, may not be relevant in the viscoelastic behaviour of the tissue they are embed in [58].

At the molecular level, the structural features of certain types of collagen fibres are relevant to the macroscopically observed mechanical behaviour of tissues [54]. One study showed that, as tissue is stretched, there is first a macroscopic straightening of fibrous kinks only later followed by such unfolding of constituting molecules [21]; the macroscopic stretching of tissue, however, is much larger than that of the molecules. Other study confirms the idea that the axis of fibrils coincides with the direction of the underlying molecules along which there is a higher stress response under nanoindentation [76]. Nonetheless, collagen fibres in connective tissues that are observed as narrow film bands seem to be isotropic, but still with highly differentiated mechanical properties with respect to those from the tissue sample they are embed in [79]. Cyclic loading, meanwhile, is capable of bringing about changes at molecular level, namely deposition of insoluble elastin onto collagen, which are associated to an observed increase in tissue stiffness and strength [36].

2.3 A Context: Long-Range Force Transmission in Tissues

Long Range Force Transmission (LRFT) in between cells of connective tissues, particularly fibroblasts, has long been documented [26, 63]. This phenomenon is related to stimulation of internal processes to the cells thus involved [9]; cell patterning scenarios, such as those underlying development of cartilage and support tissues [66, 71]; and participation in the force transfer in muscular tissues [46]. Furthermore, some harmful biological processes may also be influenced by this kind long-range mechanical stimuli, such as tumour development [18].

As with any other solid continuum structure, transmission of forces between two points in it, whereby a displacement is prescribed at such locations, takes place by stiffening of the material in between: the larger the stiffness, the higher the value of a force thus transmitted. However, to speak of a force transmission as a phenomenon of interest, there must be a markedly orientated stiffening effect in specific regions of the solid.

A first, basic stiffening effect comes from non-linear stress-strain behaviour of biological tissues. In hyperelastic materials is typical to have growths of exponential form, so that a stepped application of a prescribed displacement at points A and B will turn neighbouring regions progressively stiffer. Eventually, the material line in between A and B will become more stretched than other places of the domain, and so a preferential stiffening occurs, to which a differentiated force transmission ensues.

Given that, in addition to isolated cells, connective tissues consist of a ground substance which embeds a wide variety of fibre-like structures [41], this first mech-

anism of stiffening would turn to the isotropic nature of the ground substance itself. However, its contribution to the stiffness of the connective tissue seems not relevant, at least in animal samples of ligament and muscular fascicle [28]. Nonetheless, in a study, researchers artificially stimulated the the local stiffening of a hydrogel sample by cross-linking its polymer units [80]. This locally stiffened hydrogel, which mimicked the ground substance, led to the conclusion that such stiffenning can be relevant to certain mechanosensing processes in stem cells, which reside in embryonic connective tissue.

A second and more effective mechanism for stiffening is the fibrous second phase in the ground-substance matrix. Although first considered analytically in the design of composites for structural applications, the role of fibres on enhancing material stiffness and stress transfer thereof is also acknowledged and studied in the case of living matter [56, 72]. In this case, however, the effective mechanism by which fibres contribute to the material stiffness is not just their presence but the interaction between individual fibrils. This interaction takes place by chemical bonding of the constituent molecules of the fibres either naturally, through binders secreted by effector cells, or by external addition of reagents that reversibly attach to the fibrils. Furthermore, said interaction has also been considered in the context of ageing processes [8]. In particular, there are two chemical binding processes, one of which takes place during growth and maturation phases of living tissue, while the other one prevails during ageing. The latter is responsible for the stiffening of tissues to an extent at which it is considered deleterious.

Apart from fibre interactions by molecular binding, an important factor in the stiffening of tissues is the orientation of their fibres [74]. In one scenario, this reorientation also stimulates an increase in stiffness of the cells embedded therein [67]; this happens along the prevailing direction of the fibres, and the result is a stiffened tissue altogether. In other, related application contexts, fibre orientation is a strategy applied to tissue repairing with artificial, carbon nanotube scaffolds, whose geometric layout stimulates certain patterns of cell growth [52]. Also, soft robotics applications [47] turn to the same strategy: fibre-reinforced elastomers are designed to create highly controlled, directed motion and exertion of force. This has found applications in the creation of orthopaedic devices [6] and in procuring ventricular assistance in blood-pumping devices [55].

2.4   Work performed and organisation

In this work we consider a hyperelastic-anisotropic model of biological, connective tissue. The ground substance is modelled as a Neo-Hookean isotropic material, whereas for the anisotropic contribution to the strain energy function we considered two cases: an exponential and then a Worm-Like Chain (WLC) model. These turn to the microsphere approach to connect micro-scale description and macro-

scale continuum behaviour. Chapter 3 lays out the kinematic and the stress-and elasticity tensor foundations, whereby we establish the way in which we use the strain energy functions and the derivatives to be implemented in a user-defined subroutine facility provided by Abaqus™. Also, relevant details of the microsphere approach to modelling are commented, as well as those related to the model for fibre reorientation; there, we used the model proposed by Menzel et al. [50], which starts from a isotropic, spherical bundle of fibres, and disregards an Orientation Distribution Function, so that ODF $\rho = 1$ in this work. Section 3.4 of chapter 3 presents the main features of the mesh employed, which had to be created with a different tool to that of the finite element method solver proper; also, some notes on postprocessing are exposed, for, again, external tools were used to generate results; and then we comment on the main characteristics of the user-defined subroutine UMAT, where the strain energy functions, the stress and elasticity tensor and the updating of fibre orientation are implemented. Chapter 4 starts with an analytic solution to the 1D uniaxial tension case, whereby the main effects of individual fibre model and of the remodelling formulation parameters on stress σ_{xx} and on the amount of remodelling as indicated by a parameter proposed by Menzel et al. [50] are exposed. The second part of this chapter presents some numerical results, whereby we start with the simulation of a simple shear test and then consider the case of a plate with two holes, where a radial contraction is prescribed; these tests were run for a number of combinations of fibre model and remodelling parameter values.

3.1 Essential Kinematics

Figure 3.1 shows the kinematics of a material body $\mathcal{B}$, which is a closed set of material points. Here, κ_0 is a function of $\mathcal{B}$ that maps the set of its material points to the coordinates they occupy in space at the beginning of the deformation process; κ_t does the same mapping at a time t thereafter. The motion is characterised by the expression $\mathbf{x} = \chi(\mathbf{X}, t)$, where the motion function χ represents the transformation $\chi : \kappa_0 \longrightarrow \kappa_t$. This mapping relates the position vector $\mathbf{X}$ of a material point belonging to $\mathcal{B}$ in configuration κ_0, to its current position $\mathbf{x}$ corresponding to configuration κ_t.
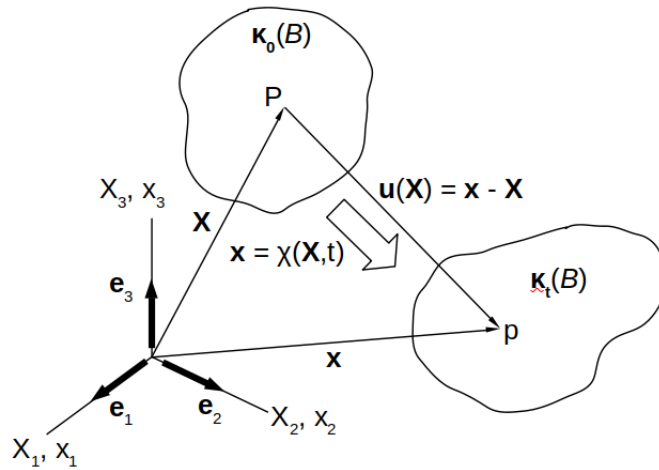

Figure 3.1: Kinematics of body $\mathcal{B}$ motion.

The deformation gradient $\mathbf{F}$ is defined as the material gradient of the deformation map $\chi(\mathbf{X}, t)$. It is a second order tensor describing the motion of continua.

$$\mathbf{F} = \nabla\chi(\mathbf{X}, t), \quad \mathbf{F} = \frac{\partial \mathbf{x}}{\partial \mathbf{X}}, \quad F_{iJ}\mathbf{e_i} \otimes \mathbf{e_J} = \frac{\partial x_i}{\partial X_J}\mathbf{e_i} \otimes \mathbf{e_J}. \tag{3.1}$$

13

Furthermore, $J := \det \mathbf{F}$ is the Jacobian of the deformation tensor, and can be used to represent a volume-preserving deformation constraint by setting $J = 1$. This one is characteristic of incompressible materials [29]. The deformation tensors employed in this document are defined on the basis of $\mathbf{F}$ and its volume-preserving counterpart $\overline{\mathbf{F}} = J^{-1/3}\mathbf{F}$.

Strain is a definition based upon measurable deformation quantities, such as elongation of rectilinear material segments or change of angle between two material segments that are originally perpendicular to each other. Moreover, such definitions must be unaltered by superimposed rigid body rotation [29].

The strain tensor used here is the right Cauchy-Green deformation tensors, $\mathbf{C}$ and its volume-preserving fraction $\overline{\mathbf{C}}$. Its original definition is cast terms of the deformation gradient $\mathbf{F}$, shown by Equation 3.2.

$$\mathbf{C} = \mathbf{F}^T\mathbf{F}, \quad \overline{\mathbf{C}} = \overline{\mathbf{F}}^T\overline{\mathbf{F}} \qquad (3.2)$$

$\mathbf{C}$ is a strain measure referred to the original configuration $\kappa_0(\mathcal{B})$ and is particularly suited to formulating constitutive equations for large strain elasticity in the context of hyperelasticity. From the point of view of computational implementation using the finite element method, however, a strain measure related to the current configuration is preferred. In actual practice, commercial finite element software that allows implementation of user-defined constitutive equations offer the analyst a programming interface; in it, he/she can write subroutines for the calculation of stress and elasticity tensor expressions for a prototype quadrature point. Part of the task in writing such a user defined subroutine is casting the resulting expressions in tensors associated to current configuration.

The ratio of the length of a material segment belonging to current configuration $\kappa_t(\mathcal{B})$ to that corresponding to the not-deformed one $\kappa_0(\mathcal{B})$ is called stretch ratio λ, and is a suitable measure of deformation from the point of view of experimental characterisation of materials and of proposing constitutive equations. Formally, λ is the Euclidean norm of a vector $\boldsymbol{\lambda}$ that is the result of the action of $\mathbf{F}$ upon a unit vector $\mathbf{a}_0$ which belongs to $\kappa_0(\mathcal{B})$, as Equation 3.3 indicates.

$$\lambda = |\boldsymbol{\lambda}| = \mathbf{F}\mathbf{a}_0 \qquad (3.3)$$

In our work, fibre orientations $\mathbf{r}_i$ take the place of the aforementioned unit vector $\mathbf{a}_0$, and allow using their individual stretch λ_i to represent 1D, micro-scale inspired strain energy functions. Their correspondence to a 3D quantity can be achieved by use of so-called structural tensors, which are set out as dyadic products (i.e. $\mathbf{r}_i \otimes \mathbf{r}_i$). Furthermore, this 3D quantity is intended to be part of a continuum, whereas the original 1D counterpart is valid at the microscale only. Such bridging of scales is called homogenisation, and this work resorts to a specific form of it called microsphere modelling. This approach is presented in section 3.2.3.

3.2 Hyperelastic Materials

3.2.1 Components of Strain Energy Function

Hyperelasticity is a theory that allows producing relationships between stress and strain with the aim of characterising the mechanical behaviour of elastic materials undergoing large deformations. Here, a strain energy function ψ is usually cast in terms of the right-Cauchy Green tensor $\mathbf{C}$ or its invariants.

The main feature of strain energy function ψ is the additive decomposition in volumetric and volume-preserving -or isochoric- contributions, $\psi = \psi_{vol} + \psi_{ich}$. As regards the volumetric part of the strain energy, the definition $J = \det \mathbf{F}$ implies the expression $\psi_{vol} = \psi_{vol}(J)$. On this basis, these models must comply with the normalisation condition $\psi_{vol}(1) = 0$ and, then, fit experimental results with as few empirical parameters as possible; moreover, these should convey a physical interpretation. Then again, if the material is incompressible, there is no volumetric strain energy function, and the stress contribution is just the hydrostatic pressure p times the identity matrix. In that regards, the implementation used in this work allows considering a compressible matrix -though this condition was not employed actually-, whose strain energy function is given by Equation 3.4. Incompressibility can be enforced by using a large value for the parameter κ therein.

$$\psi_{vol}(J) = \frac{2J}{\kappa}\left(\frac{J}{2} - 1\right), \tag{3.4}$$

Regarding ψ_{ich}, it is also additively split into an isotropic ψ_{iso} and an anisotropic ψ_{ani} contribution parts; for the former, we use the *Neo-Hookean* strain energy function that represents the ground substance, and it is given by Equation 3.5, where I_1 is the first invariant of $\mathbf{C}$ and C_{10} is an empirical, material dependent parameter directly related to its stiffness.

$$\psi_{iso} = C_{10}(I_1 - 3) \tag{3.5}$$

Meanwhile, the specific definition of ψ_{ani} can follow different approaches. In general, they start from the definition of a structural tensor as the dyadic product of unit, material vectors $\mathbf{a}_0$. Sometimes, these products $\mathbf{a}_0 \otimes \mathbf{a}_0$ are used to formulate special invariants of deformation tensors [29]; others multiply said product by other terms intended to capture features like fibre dispersion [2]. For instance, Gasser et al. [23] propose the concept of Generalised Tensor $\mathbf{H} := \mathbf{a}_0 \otimes \mathbf{a}_0$; the strain energy function is then the product of $\mathbf{H}$ and an Orientation Density distribution Function (ODF) ρ of a family of $i = 1...n$ fibres. This is centred around a preferred orientation given by the unit vector $\mathbf{a}_0$ in the reference configuration.

Another approach proposes strain energy functions at the individual fibre level [2], what enables consideration of phenomenological and of micromechanical models of collagen fibre behaviour. In this approach the strain energy function for a

family I of $i = 1...n$ fibres, i.e. ψ_f^i, is expressed as the average over a unit sphere $\mathbb{U}^2$ of n fibres per unit volume times the ODF ρ times a strain energy function of a single fibre. In this work, however, we consider that fibres start from an isotropic state, i.e. they are uniformly distributed over the surface of a sphere, and do not turn to an ODF to establish its distribution at any time throughout the analysis. In other words, $\rho = 1$. Furthermore, we also consider only one family of fibres, so that the resulting strain energy function is as shown in Equation 3.6.

$$\psi_{ani} = \sum_i < n\psi_f^i(\overline{\lambda}) >, \quad < n\psi_f^i(\overline{\lambda}) >= \frac{1}{4\pi} \int_{\mathbb{U}^2} n\psi_f^i(\overline{\lambda}) dA \qquad (3.6)$$

3.2.2 Constitutive models for individual fibre behaviour

Generally speaking, it is assumed that fibres do not oppose compressing action, so that their strain energy function equates zero whenever $\lambda < 1$. For $\lambda \geq 1$, there are at least two expressions representing the energy accumulation according to the amount of stretching [2]: the exponential or phenomenological model, that imitates the observed resistance in the stretching of rubber-like materials; and the Worm-Like Chain model (WLC), that relies on a micromechanical model inspired on the molecular structure of the collagen fibres.

Exponential model

In this case the strain energy function of ith fibre is given by Equation 3.7 [2, 30].

$$\psi_f^i = \frac{k_1}{2k_2}[\exp(k_2[\lambda_i^2 - 1]^2) - 1] \qquad (3.7)$$

A simple plot of an exponential function of the form given in Equation (3.7) shows that the material parameter k_1 just scales the response at every value of stretching λ_i, whereas an increase k_2 forces most of the response to take place at the largest values of stretch, see Figure 3.2. This could be use to fit experimental observations like those reported by Roach et al. [60], whereby collagen is considered very stiff and thus contributes little to tissue stresses at low stretches, much unlike elastin fibres; at high stretches, the response is almost exclusively due to collagen, and so small stretch increases in this region bring about large stresses. The aforementioned role of k_1 could be linked to the initial slope of the stress-stretch curve, a parameter employed by some researchers to refer to different tissue conditions [1, 16, 69].

Worm-Like Chain (WLC) model

In a WLC approach the collagen fibre is modelled as a discrete-point assemblage that represents one or more of its constituent molecules. The principles of statistical mechanics can be used to give mathematical form to the strain energy function.
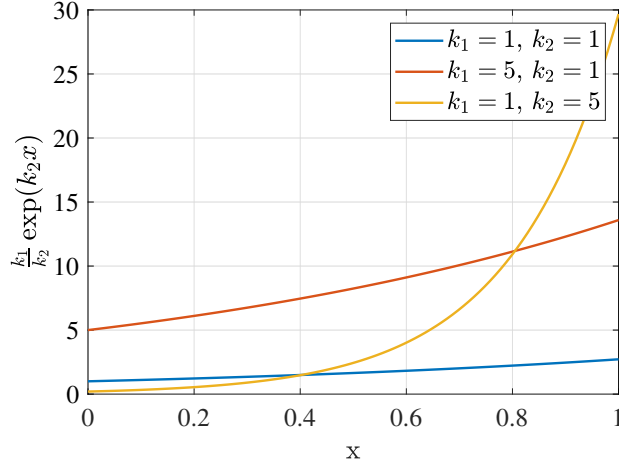
Figure 3.2: Effect of parameters k_1 and k_2 in an exponential function.

In particular, a probability distribution function of the most likely configuration is laid out, upon which a function for the energy associated to changing that configuration emerges. In this work we use the specialisation of the eight-chain model from Arruda et al. [4] to transversely isotropic materials. This particularisation produces a strain energy function for a 1D stretching of the fibre, according to Equation 3.8 [2, 3].

$$\psi_f^i = \frac{nK\Theta L}{4A}\left(2\frac{\bar{r}_i^2}{L^2} + \frac{1}{1 - \bar{r}_i/L} - \frac{\bar{r}_i}{L} - \frac{\ln\lambda^{4r_0^2}}{4r_0 L}\left[4\frac{r_0}{L} + \frac{1}{[1 - r_0/L]^2} - 1\right] - \psi_r\right). \quad (3.8)$$

In Equation 3.8 $B := \frac{1}{4}nK\Theta r_0/A$ is taken as a material dependent parameter [2]; r_0 is the length of the ith non-stretched molecular chain -here one molecular chain represents one fibre, according to the affine deformation concept- and L is the maximum length attainable by a chain. Furthermore, $\bar{r}_i := \lambda_i r_0$; and $\psi_r = 2r_0^2/L^2 + [1 - r_0/L]^{-1} - r_0/L$ is an energy term which accounts for a nonzero, initial strain energy at zero stretch. It is important to note that r_0 and L pose a limit to the stretch that each chain can have in this model, namely $\lambda_{max} = L/r_0$.

3.2.3 The microsphere modelling approach

It is a numerical homogenisation technique whereby models of matter at microstructural level can be gathered into an equivalent contribution valid at the continuum level. At the micro-scale level, discrete features of matter such as molecular structure are the subject of direct modelling. At that size scale, this way of addressing material modelling takes the form of 1D representations of relatively simple assemblies of chain molecules based on kinetic theory or statistical mechanics, or just continuum 1D, rod-like elements following a phenomenological

response of matter.

The microsphere approach can be seen as based on the microplane concept, whereby direction-dependent response of materials is captured by considering a polyhedron at every quadrature point in a finite element scheme. According to [12], the normal to the polyhedron facets represent the response of the material in that specific direction, in what would be a micro-scale interpretation of the material behaviour. To recover an equivalent macro-scale response, the polyhedron is circumscribed into a unit sphere. The segments between the sphere centre and the polyhedron vertices and mid-edge points are the quadrature vectors for integration over the sphere.

There are several criteria as to the quadrature directions that lead to optimum integration [7, 10] in the sense of the accuracy obtained given a number of integration directions, and of how this ratio depends on proper selection of such directions and on the nature of the function being integrated.

In the context of the microsphere approach, the unit sphere $\mathbb{U}^2$ is addressed directly, without resource to the aforementioned polyhedron, and the integration directions are associated to the physical fibres of the biological tissue [50]. Here, a typical part of the integrand is an orientation distribution function (ODF) ρ, which is a continuous, spherical function, the Bingham model being one such case [62]. Here, the accuracy of the integral is significantly influenced by the choice of the set of integration directions [2].

As mentioned earlier, in this work we employed a uniform distribution of fibres, i.e., ODF $\rho = 1$, so that application of the microsphere approach consists of the numerical integration of the expression in Equation (3.6). To be specific, we recognise that the stretch λ is both argument of the function to be integrated, and function of the fibre orientations $\mathbf{r}$. Then, the integration takes place at every quadrature point of the continuum formulation, in a finite element context, and is the sum of the function to be integrated evaluated at specific points within the domain times a corresponding weight. In particular, we used a set of 184 integration directions also uniformly spaced over the sphere surface, following the work of Alastrue et al. [2]. In this way, the integration scheme is that shown in Equation (3.9).

$$< g(\mathbf{r}) >= \int_{\mathbb{U}^2} g(\mathbf{r}) dA \approx \sum_i^n w^i g(\mathbf{r}_i) \tag{3.9}$$

3.2.4 Calculation of stress and elasticity tensor

Stress tensor

Stress is defined as the ratio of internal force vector at a material point to the oriented unit area element. If its orientation unit vector is $\mathbf{n}$, and the force per unit area, or traction, is denoted as $\mathbf{t}$, then the Cauchy stress tensor σ is defined by Equation 3.10. On this basis, Cauchy stress is a measure associated to current configuration, and is the one used to cast actual results in almost any engineering analysis.

$$\mathbf{t} = \boldsymbol{\sigma}\mathbf{n}. \tag{3.10}$$

Multiplication of $\boldsymbol{\sigma}$ by the determinant J does not affect the properties of a stress tensor, and is indeed another stress measure, called Kirchoff stress $\boldsymbol{\tau}$, again related to configuration $\kappa_t(\mathcal{B})$, Equation 3.11. For this work, the original result of the first derivative of the strain energy contribution from reinforcing fibres is cast in this stress measure [2].

$$\boldsymbol{\tau} = J\boldsymbol{\sigma} \tag{3.11}$$

Nevertheless, when reference is made to the fibre orientation $\mathbf{r}_i$ before it is acted upon by the deformation gradient tensor, as was the case in our work, the stress measure thus produced is the second Piola-Kirchoff. Equation 3.12 indicates its relation to the Cauchy stress.

$$\mathbf{S} = \mathbf{F}^{-1}\mathbf{P}, \quad \mathbf{S} = J\mathbf{F}^{-1}\boldsymbol{\sigma}\mathbf{F}^{-T} \tag{3.12}$$

Stress tensor $\mathbf{S}$ does not admit a straightforward interpretation from the point of view of the verbal definition of stress [29]; the purpose of its definition is to assist the implementation of numerical solution to problems with hyperelastic materials.

Stress tensor comes from differentiation of the strain energy function with respect to some strain measure. The formulations will be presented in terms of stress and strain measures referring to the current configuration, while some parts of the actual implementation used in this work may turn temporarily to measures associated to the material configuration.

The main feature is the volumetric-isochoric additive split of the strain energy: $\psi(\mathbf{b}) = \psi_{vol}(J) + \psi_{ich}(\overline{\mathbf{b}})$. Although the material is considered incompressible in this work, the formulations have an explicit term for ψ_{vol}; here, incompressibility is enforced by setting a large value for parameter κ in Equation 3.13.

$$\psi_{vol}(J) = \kappa J(\frac{J}{2} - 1) \rightarrow \frac{d\psi_{vol}}{dJ} = \kappa(J - 1). \tag{3.13}$$

The volumetric Cauchy stress can be calculated from the derivative of the strain energy function according to Equation (3.14).

$$\boldsymbol{\sigma}_{vol} = 2J^{-1}\frac{d\psi_{vol}}{dJ}\frac{\partial J}{\partial \mathbf{b}}\mathbf{b} = 2J^{-1}\frac{d\psi_{vol}}{dJ}\frac{J}{2}\mathbf{b}^{-1}\mathbf{b} = \frac{d\psi_{vol}}{dJ}\mathbf{I}, \tag{3.14}$$

where $\mathbf{I}$ is the second order unit tensor.

As regards the volume-preserving Cauchy stress $\boldsymbol{\sigma}_{ich}$, the derivative with respect to isochoric strain measure $\overline{\mathbf{b}}$ follows Equation(3.15).

$$\boldsymbol{\sigma}_{iso} = 2J^{-1}(\frac{\partial\psi_{iso}(\overline{\mathbf{b}})}{\mathbf{b}})\mathbf{b} = 2J^{-1}(\frac{\partial\psi_{iso}(\overline{\mathbf{b}})}{\overline{\mathbf{b}}}\frac{\partial\overline{\mathbf{b}}}{\partial\mathbf{b}})\mathbf{b}. \tag{3.15}$$

ψ_{iso} corresponds to the contribution from the isotropic matrix and it is modelled by a Neo-Hookean material model, $\psi = C_{10}(I_1 - 3)$, where C_{10} is a material dependent parameter and I_1 is the first invariant of $\mathbf{b}$. Its relation to the first invariant of $\overline{\mathbf{b}}$, i.e. $\overline{I}_1$ is given by $I_1 = J^{-2/3}\overline{I}_1$, and so we can establish that $\psi_{iso}(\overline{\mathbf{b}}) = \psi_{iso}(\overline{I}_1)$; we can then simply substitute $\partial\psi_{iso}(\overline{\mathbf{b}})/\partial\overline{\mathbf{b}}$ by $\partial\psi_{iso}\overline{I}_1/\partial\overline{I}_1$ in Equation 3.15. Application of the identity for $\partial\overline{\mathbf{b}}/\partial\mathbf{b}$ [29] leads to Equation (3.16).

$$\boldsymbol{\sigma}_{iso} = \mathbb{P}_s : \overline{\boldsymbol{\sigma}}_{iso}, \tag{3.16}$$

where $\mathbb{P}_s = \mathbb{I} - \frac{1}{3}\mathbf{I}\otimes\mathbf{I}$ is the fourth order spatial projection tensor, and $\mathbb{I}$ is the fourth-order identity tensor [29]. Also, $\overline{\boldsymbol{\sigma}}_{iso}$ is the so-called fictitious Cauchy stress tensor, and is given by Equation (3.17).

$$\overline{\boldsymbol{\sigma}}_{iso} = 2J^{-1}(\frac{\partial\psi_{iso}(\overline{I}_1)}{\partial\overline{I}_1})\overline{\mathbf{b}} \tag{3.17}$$

Finally, for the anisotropic stress contribution $\boldsymbol{\sigma}_{ani}$, the actual implementation calculates first the so-called fictitious second Piola-Kirchoff stress $\overline{\mathbf{S}}_{ani}$, which turns to the first order differentiation of $\psi_f(\overline{\lambda})$, as given by Equation (3.18) [2].

$$n\frac{\partial\psi_f^i}{\partial\overline{\lambda}_i} = B\left(4\frac{r_0}{L}\left[\overline{\lambda}_i - \frac{1}{\overline{\lambda}_i}\right] + \frac{1}{[1 - \overline{r}_i/L]^2} - \frac{1}{\overline{\lambda}_i[1 - r_0/L]^2} + \frac{1}{\overline{\lambda}_i} - 1\right) \tag{3.18}$$

Then $\overline{\mathbf{S}}_{ani}$ is given by Equation (3.19),

$$\overline{\mathbf{S}}_{ani} = < n\frac{\partial\psi_f^i}{\partial\overline{\lambda}}\overline{\lambda}_i^{-1}\mathbf{r}\otimes\mathbf{r} > \tag{3.19}$$

where $\mathbf{r}$ is a continuous function to describe the fibre orientation.

In the context of the microsphere approach to modelling, $\mathbf{r}$ is treated as a discrete set $\mathbf{r}_i$, where i simultaneously represents integration directions and physical fibre directions, following the arguments from the work of Menzel et al. [50]. Furthermore, the brackets indicate the operation of averaging over a unit sphere; the arguments inside the brackets are the integrand thereof.

The implementation used in this work calculates the anisotropic Cauchy stress from $\overline{\mathbf{S}}_{ani}$ using the Equation (3.20), where $\mathbb{P}_m = \mathbb{I} - \frac{1}{3}(\mathbf{C}^{-1} \otimes \mathbf{C})$ is the material fourth order projection tensor [29]. The result of this calculation, when implemented in a user subroutine, is passed back to the finite element software at every quadrature point.

$$\boldsymbol{\sigma}_{ani} = J^{-1}\overline{\mathbf{F}}(\mathbb{P}_m : \overline{\mathbf{S}}_{ani})\overline{\mathbf{F}}^T, \tag{3.20}$$

Elasticity tensor

Although the software where we implemented the material model is a subroutine that must return stress and elasticity tensor in current configuration measures, the theoretical formulations can be presented in either the current or the original one. In this section we present the elasticity tensor main expressions using measures associated to the reference or material configuration.

The elasticity tensor is just the differentiation of stress, for instance $\mathbb{C} = 2\partial\mathbf{S}/\partial\mathbf{C}$; additionally, the additive split into volumetric and isochoric contribution is also applied, i.e. $\mathbb{C} = \mathbb{C}_{vol} + \mathbb{C}_{iso}$. From the result that $\mathbf{S}_{iso} = Jp\mathbf{C}^{-1}$ [30], then $\mathbb{C}_{vol}$ is given by Equation (3.21),

$$\mathbb{C}_{vol} = J\tilde{p}\mathbf{C}^{-1} \otimes \mathbf{C}^{-1} - 2Jp\mathbf{C}^{-1} \odot \mathbf{C}^{-1} \tag{3.21}$$

where the product $\mathbf{C}^{-1} \odot \mathbf{C}^{-1}$ is defined in the work of Holzapfel [29]. Also, $\tilde{p}$ is short for $p + Jdp/dJ$ and $p = d\psi_{vol}/dJ$.

As regards the expression for $\mathbb{C}_{iso}$, though it straightforwardly follows from derivation of the expression for $\mathbf{S}_{iso}$, obtained in turn from $\boldsymbol{\sigma}_{iso}$ (Equation (3.16)) and Equation(3.12), it is a set of terms obtained from a rather lengthy derivation process[1]. However, the end result is the form given by Equation(3.22), and is the way in which it is coded in the user subroutine UMAT used in this work.

$$\begin{aligned}
\mathbb{C}_{iso} = {}& \mathbb{P}_m : \overline{\mathbb{C}} : \mathbb{P}_{4M}^T + \frac{2}{3}\mathrm{Tr}(J^{2/3}\overline{\mathbf{S}})\tilde{\mathbb{P}} \\
& - \frac{2}{3}(\mathbf{C}^{-1} \otimes \mathbf{S}_{iso} + \mathbf{S}_{iso} \otimes \mathbf{C}^{-1})
\end{aligned} \tag{3.22}$$

In Equation (3.22), the term $\overline{\mathbb{C}}$ is the fictitious material elasticity tensor, and contains the double derivative $\partial\psi_{iso}^2/\partial^2\overline{\mathbf{C}}$, whereby the specific strain energy function is substituted. In this work, this approach is used to consider the Neo-Hookean, isotropic ground substance.

The anisotropic contribution $\mathbb{C}_{ani}$ comes from the second differentiation of the strain energy function for the 1D fibre model, according to the expression derived by Alastrue et al. [2] and shown in Equation (3.23).

---

[1]The details are presented in the Example 6.8 in reference [29].

$$n\frac{\partial^2 \psi_f^i}{\partial \overline{\lambda}_i^2} = B\left(\frac{1}{\overline{\lambda}_i^2}\left[4\frac{r_0}{L} - 1 + \frac{1}{[1 - r_0/L]^2}\right] + \frac{2r_0}{L[1 - \overline{r}_i/L]^3} + 4\frac{r_0}{L}\right) \tag{3.23}$$

Then, the fictitious material elasticity tensor incorporates Equation (3.23) as shown in Equation (3.24).

$$\overline{\mathbb{C}}_{ani} = <n(\lambda^2\frac{\partial^2 \psi}{\partial \lambda^2} - \lambda\frac{\partial \psi}{\partial \lambda})\mathbf{r} \otimes \mathbf{r} \otimes \mathbf{r} \otimes \mathbf{r} > \tag{3.24}$$

The strain energy function for the fibre contribution ψ_f^i is one that is cast in terms of a single stretch value.

Even though not explicitly exposed in the work of Alastrue et al. [2], it could be said that ψ_f^i is but a conventional energy function written in terms of deformation stretches, whereby λ_1 corresponds to the stretch of the fibre, and $\lambda_2 = \lambda_3 = 1$, for the model for the fibre only considers its elongation. This same rationale can be applied to the derivation of the fictitious stress $\overline{\mathbf{S}}_{ani}$ (Equation (3.19)). The details of the operation and, in particular, the emergence of the dyadic products among fibre orientations $\mathbf{r}$ are encompassed by the process called spectral decomposition of stress and of elasticity tensor [29].

3.3 Remodelling Effects

When a material is deemed elastic, any amount of energy applied to it is returned in the same quantity once the external forces or prescribed displacements are removed. Internally, this means that the material structure has not undergone any change. However, one key interest of this work lies on the effect that external forces or displacements have on the degree of anisotropy of a model biological tissue. The degree of anisotropy is directly related to the microstructure of the material, particularly the way fibrils are dispersed as a consequence of applied deformation.

When there is a change in an internal variable of the material, one part of the input mechanical energy is lost or dissipated. For a system from which energy is lost, this dissipation is a scalar quantity $D_{in} \geq 0$, according to the second law of thermodynamics. In an elastic material, this quantity is equal to the rate of work (power) exerted by internal forces, given by $\mathbf{S} : \mathbf{C}$.

To incorporate fibre reorientation and anisotropy gain thereof, the dissipation is expressed simply as $D_{in} := \mathbf{S} : \mathbf{C} - \dot{\psi}$, where ψ is the strain energy function; this function ψ is then declared to be function of the internal variables. They must be able to track the evolution of the anisotropy, and here we find several possibilities. One of the simplest consists on taking the orientation distribution function $\rho = 1$, so that both fibre dispersion and preferred orientation are totally defined by the

evolution of their individual directions $\mathbf{r}_i$; thus we have $\psi = \psi(\mathbf{r}_i)$[50].

Hence, the term $\dot{\psi}(\mathbf{r}_i)$ is equivalent to $\partial\psi/\partial\mathbf{r}_i \cdot \dot{\mathbf{r}}_i$, and indicates there must be a rate expression for the internal variable $\mathbf{r}_i$, whose integration produces the value of $\mathbf{r}_i$ that determines the value of stress $\mathbf{S}_{ani}$ and elasticity tensor $\mathbf{C}_{ani}$ at any time throughout calculations.

Menzel et al. [50] stresses that, strictly speaking, remodelling processes in living tissues are inevitably tied to growth. This says that a theoretical frame whereby mass and energy can enter the analysis volume is a more appropriate set to formulate a remodelling model.

Furthermore, the observed interaction among fibres and between fibres and ground substance means that the strain energy function for the fibre should depend on a non-affine statement of deformation.

3.3.1 Evolution equation for internal variables

In this work we follow the formulation proposed by Menzel et al. [50] whereby $\mathbf{r}_i$ is the only internal variable; other authors, for instance from Saez et al. [62] turn to both $\mathbf{r}_i$ and to the orientation of a preferred orientation of a set of fibrils -represented by an orthogonal tensor $\mathbf{Q}$- as internal variables.

The fact that we take ODF $\rho = 1$ means that our implementation does not provide a preferred orientation to the set of fibres. Furthermore, the set of integration directions, which are the same set of vectors $\mathbf{r}_i$, correspond to a uniform, isotropic spherical distribution and act out as starting condition of the material. Rather, the model from Menzel et al. [50] ties the evolution of $\mathbf{r}_i$ to the degree of deformation of the surrounding material, as indicated by the eigenvectors of the right-Cauchy Green tensor $\overline{\mathbf{C}}$.

When looking at the term $\partial\psi/\partial\mathbf{r}_i \cdot \dot{\mathbf{r}}_i$, the part $\partial\psi/\partial\mathbf{r}_i$ represents a force, according to Equation 3.25.

$$\frac{\partial\psi}{\partial\mathbf{r}_i} = \frac{\partial\psi}{\partial(\overline{\lambda}^2)}\frac{\partial(\overline{\lambda}^2)}{\partial\mathbf{r}_i} = -\overline{S}_i\overline{\mathbf{C}}\cdot\mathbf{r}_i \tag{3.25}$$

Hence, the expression for $\dot{\mathbf{r}}_i$ is taken as a projection of said force so that it is perpendicular to $\mathbf{r}_i$. Moreover, this consideration complies with the requirement that $\mathbf{r}_i\cdot\mathbf{r} = 0$. The projection of the force is obtained by application of the projection operator, so that $\mathbf{r}_i$ is given by Equation 3.26.

$$\dot{\mathbf{r}}_i = f_i[\mathbf{I} - \mathbf{r}_i \otimes \mathbf{r}_i] \cdot \overline{\mathbf{C}} \cdot \mathbf{r}_i \tag{3.26}$$

This model for $\dot{\mathbf{r}}$ indicates that as $\overline{\mathbf{C}}\cdot\mathbf{r}_i = 0$ when $\mathbf{r}_i$ matches one of $\overline{\mathbf{C}}$ eigenvectors, then these same eigenvectors constitute the horizon towards the reorientation

process moves. Furthermore, the operator $\mathbf{I} - \mathbf{r}_i \otimes \mathbf{r}_i$ represents the projection of $\dot{\mathbf{r}}_i$ onto $\mathbf{r}_i$ and is a factor that establishes how fast remodelling takes place.

As regards the weighting factor f_i, it is also defined in terms of the extent of gained anisotropy. To this end, the structural tensor A is defined by Equation 3.27.

$$\mathbf{A} = \sum_{i=1}^{m} w_i \mathbf{r}_i \otimes \mathbf{r}_i = \sum_{j=1}^{3} A_j \mathbf{n}_j \otimes \mathbf{n}_j, \tag{3.27}$$

where A_j are the eigenvalues of $\mathbf{A}$. As the natural tendency for eigenvalues of a matrix is to increase the difference A_Δ between smallest and largest values, say A_1 and A_3, then it is considered that $\mathbf{r}_i$ will evolve as long as said difference stays above some preset threshold or saturation value A_Δ. Furthermore, evolution can also be constrained to each fibre being under a state of stretch above some limiting value $\overline{\lambda}_c$. With these considerations, the criterion to calculate f_i can be stated as shown by Equation 3.28.

$$f_i = \begin{cases} 0, & \overline{\lambda}_i \leq \overline{\lambda}_c \\ \frac{A_\Delta - [A_1 - A_3]}{t^* A_\Delta}, & \text{else.} \end{cases} \tag{3.28}$$

The latter case in Equation (3.28) can also be rewritten as $\frac{1}{t^*}(1 - \frac{|A_1 - A_3|}{A_\Delta})$, which highlights the limiting role that A_Δ plays. Meanwhile, t^* is a time relaxation-like parameter.

The calculation of current value of $\mathbf{r}_i$ can follow from an integration scheme applied to Equation 3.26; for instance, an Euler-type method, as Equation 3.29 shows.

$$\tilde{\mathbf{r}}_i^{n+1} = \mathbf{r}_i^n + \Delta t f_i(\overline{\mathbf{C}}^{n+1}, \mathbf{r}_i^n)[\mathbf{I} - \mathbf{r}_i^n \otimes \mathbf{r}_i^n] \cdot \overline{\mathbf{C}}^{n+1} \cdot \mathbf{r}_i^n \tag{3.29}$$

The form in Equation (3.29) was the one actually implemented in this work; nonetheless, Menzel et al. [50] suggest that more accurate integration schemes which incorporate specific features of the problem could be applied. Among those features we can name the rotating motion of a unit vector in space, and the exponential-like evolution of load-deflection responses typically observed in biological tissues. The former case can find motivation in the simulation of motion in interconnected rigid body dynamics [13]; the latter, in the integration of constitutive equations in plasticity [70].

3.4 Numerical Implementation

3.4.1 General Pre- and Postprocessing Features

For this work we used the user defined subroutines facility from Abaqus™. Specifically, we coded the calculation of stress tensor, elasticity tensor and fibre re-

modelling as a Fortran subroutine UMAT. Some other user subroutines were also required for ancillary tasks: SDVINI to invoke the file with the set of initial fibre orientations (set of 184 unit vectors in $\mathbb{R}^3$) and the set of weights to apply to each of them, according to the microsphere setting for multiscale modelling; and UEXTERNALDB, to enable extraction of quantities for post-processing at the end of every increment.

Quantities for post-processing phase are generated automatically by Abaqus™ at the element quadrature points. We considered the following quantities for post-processing purposes: the deformation gradient tensor **F** (nine entries), the Cauchy stress tensor σ (six entries), the Cartesian coordinates of every quadrature point per element (three entries), the set of 184 unit vectors for fibre orientation and the value of the anisotropy gain parameter $|A_1 - A_3|$.

The availability of output data just at quadrature points demanded their extrapolation to the element nodes. To this purpose, a postprocess Matlab™ file was created that reads the Abaqus™ input file (extension .inp) data regarding element connectivity and node coordinates; it then reads the output files prompted by UMAT; and finally uses the Lagrange shape functions for an eight-node hexahedron to produce the corresponding value at the nodes. A loop over the mesh nodes picks the available values of quantities contributed by elements sharing any given node and produces their unweighted average value. These values are passed on to a function inside the same postprocess Matlab™ .m file, that is in charge of creating .vtk files to be read and displayed by Paraview™.

Given that simulations were run remotely on the UPC-Titani server, use of Abaqus™-CAE was not practical. Fine meshes were produced locally with gmsh™ application. This made us devise specific procedures to exclude spurious nodes before generating the .inp file to be read by Abaqus™. Furthermore, as regards the postprocess, the extrapolation .m file was hard-wired to a given mesh, so creation of another .m file in charge of reading the input .inp was required. For the case of fine meshes of the plate with two holes case, the extrapolation code had to be refactored and vectorised, so that data for visualisation could be generated within reasonable times.

For the plate with two holes case, we employed two meshes to calculate results: a rough mess with 2116 elements (Figure 3.3), to run a screening over a range of values for the material properties, and a fine one, with 68290 nodes (Figure 3.4), to see the smooth evolution of quantities between the hole edge and the plate centre.

The aforementioned post-processing procedure and files were in charge of generating the stress distribution plots for the parameter-screening stage presented in the the Results section. But plotting the fibre pattern taken on by the set of fibres as a consequence of remodelling was also a requirement, at least at some specific locations within the mesh.
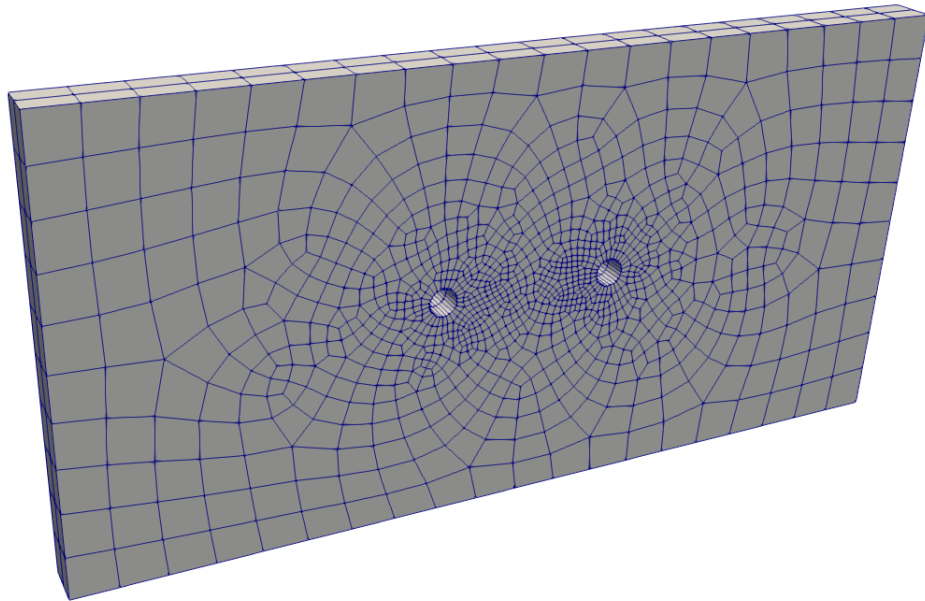
Figure 3.3: Mesh of 2116 C3D8H hexahedral elements. This mesh was employed for screening over a large number of parameter combinations.
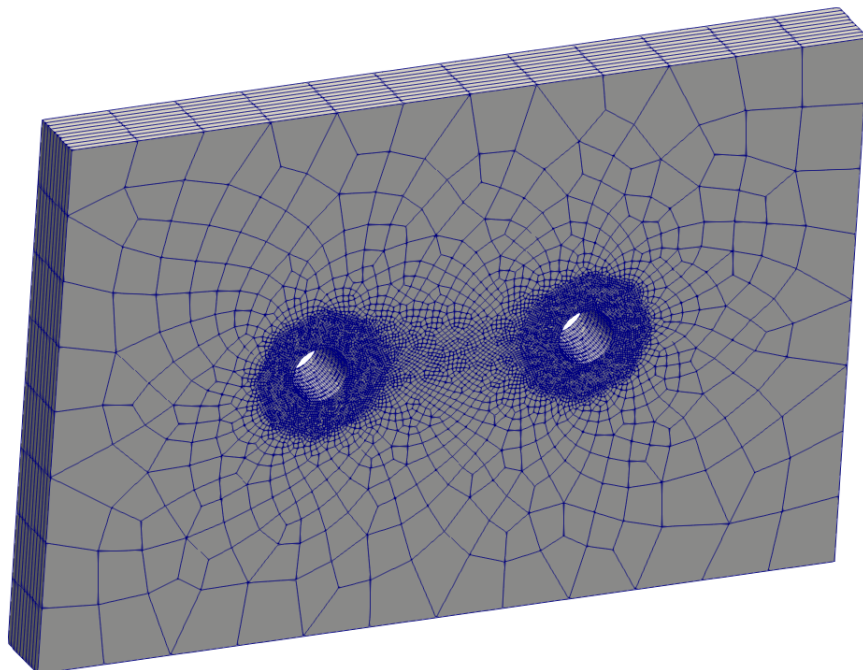

Figure 3.4: Mesh of 68290 C3D8H hexahedral elements. Mesh refinement was set to be symmetric with respect to the hole centres.

Here, a set of instructions within the UEXTERNALDB and the UMAT sub-routines generated another output file, IVARIA*.out, where $*$ is an index for the number of increment where the set of 184 fibre orientations at each quadrature point was produced. These files were too large in size to consider copying them all from Titani server to our local machine. For instance, the rough mesh for the plate with two-holes used in the parameter screening stage of the study case, consisted of 2116 element or 16928 quadrature points; along with the need for double precision figures, this led to files of about 196 MB size for each (converged) increment.

So, a small shell script was created here to pick the set of 184 fibre orientations from a selected element and a quadrature point in it. That shell script was run in Titani server and produced a much smaller $\approx$ 12 KB file for each increment.

To select the elements at whose locations we wanted getting the fibre deformation patterns, we first plotted the whole mesh in Paraview™ and used the facilities of its graphical interface to identify the index for a set of elements lying along the segment that connects the plate hole centres. Nonetheless, only one quadrature point was selected, namely #1, as automatically assigned by Abaqus™ ; this fact led to inaccuracies particularly in the element on the hole edge, where gradients of calculated quantities were significant. This fact also motivated the analysis of the plate with two holes case using a much finer mesh (68290 elements), which should only be carried out for a few selected combination of material properties.

Plotting of the set of 184 fibres, however, did not require extrapolation from values at quadrature points to values at element nodes; we created a post-processing .m file that reads the entries of $\overline{\mathbf{F}}$ at the element and quadrature point number where the set of 184 fibre orientations $\mathbf{r}_i$ were produced by the aforementioned shell script, and calculated the product $\overline{\mathbf{F}}\mathbf{r}_i$. The resulting vector was passed on to a .vtk file generating function and read as though these directions were 1D elements of a mesh; so were these read and displayed in Paraview™.

For the parameter-screening stage of the study, it was in our interest plotting the variation of stress components σ_{11}, σ_{22} and σ_{12}, and of anisotropy parameter $|A_1 - A_3|$ along the selection of elements between the hole centres of the plate. Doing that on our local machine would require copying the entirety of the output files produced by Abaqus™ ; so, in similar fashion to the management of the large fibre-orientation files IVARIA*.out, we created a shell script that was run in Titani and extracted the required stress components and value of $|A_1 - A_3|$ for the selected elements and their quadrature point #1. Again, this led to inaccuracies at the element on the hole edge, due to potentially significant differences when going from one quadrature point to the next.

3.4.2 Finite Element Method

Abaqus™Interface

In our work, Abaqus™ is in charge of producing the interface for the finite element method, up to the point of generating the calculation expressions that take place at every quadrature point. The interface corresponds to producing an approximate solution to a variational problem for the quasi-static balance of momentum for a solid mechanics problem. In this regards, the internal-variable nature of the remodelling model employed in this work, was taken as a pseudo-time delayed equilibrium response.

Within each increment the equilibrium response is calculated iteratively, for the problem is nonlinear due to the hyperelastic material behaviour and the presence of large strains. Here, a conventional Newton-Raphson method is employed. This is worth mentioning, for the load deflection curve in certain boundary value problems with hyperelastic materials, for instance that of balloon inflation, exhibits load-softening at some point throughout the inflation process [29]. In this case, the load-deflection curve does not grow monotonically, but features a local maximum, whereby the classical Newton method would fail to converge. Special solution methods would be required here, for example, one of those belonging to the line-search category [11].

The element utilised in this work is a eight-node hexahedron of hybrid type, named C3D8H in Abaqus™. It has the three Cartesian components of displacement as nodal variables and one value of pressure at the middle of the element volume. Schoenherr et al. [64] propose a new hybrid element and uses, among others, C3D8H element as benchmark, whereby convergence and stability are shown to depend on the loading condition and the material model. A wider elaboration on the capabilities and failure scenarios for hybrid finite elements can be found in the work of Hughes [33].

Governing equations

For the problem at hand, the virtual work V is a nonlinear function of the set of material point displacements $\mathbf{u}$; its solution consists of the iterated solution of a linear approximation to V, as dictated by a Taylor series expansion: $V(\mathbf{u}_1) \approx V(\mathbf{u}_0) + \Delta V(\mathbf{u}_0)$.

The virtual V_i work due to internal forces, in the context of a large deformation problem, can be cast for the body in the original, or reference, configuration Ω_0. As dimensions of work and energy are the same, V_i can be expressed as the product of a strain, a stress measure and a differential element $d\Omega_0$, as shown in Equation 3.30.

$$V_i = \int_{\Omega_0} \mathbf{S}\delta\mathbf{E}d\Omega_0, \tag{3.30}$$

where $\mathbf{S}$ is the second Piola-Kirchoff stress tensor, and $\mathbf{E}$ is the Green strain tensor.

In our work, external forces or those arising by prescribed displacements do not change with body deformation, $\Delta V = \Delta V_i$. In this case ΔV_i is given by Equation 3.31 [17].

$$\Delta V_i = \int_{\Omega_0} (\delta\mathbf{E}^T\mathbf{C_{SE}}\delta\mathbf{E}) + (\mathbf{S} : \delta\mathbf{D}^T\delta\mathbf{D})d\Omega_0, \tag{3.31}$$

where $\mathbf{C_{SE}}$ is the fourth-order constitutive tensor that relates $\mathbf{S}$ and $\mathbf{E}$. This tensor comes from the second differentiation of the strain energy function ψ with respect to strain, whereas $\mathbf{S}$ is computed from the first derivative of ψ. The specific expressions for these two quantities are to be implemented in UMAT; $\mathbf{D} = \mathbf{F} - \mathbf{I}$ is the displacement gradient tensor.

The basic way in which UMAT contents are implemented allow considering a compressible hyperelastic material model, by means of an explicit declaration for a volumetric strain energy along with a compressibility material parameter (declared in the input .inp file). However, our work instructs Abaqus™ using the C3D8H mixed element, which enforces incompressibility, while incorporating hydrostatic pressure p as an unknown to the finite element problem.

So, the linearised finite element problem to be solved reduces to $0 = (V_i + V_e) + (\Delta V_i)$, where V_e is the virtual work due to prescribed tractions or, as is our case, forces associated to prescribed displacements. Crisfield [17] provides a complete account of the matrix formulation for specific element discretisations.

3.4.3   UMAT structure

The most important guiding feature here was the implementation of the remodelling model. As it was finally written, it starts by picking up the set of 184 initial-state unit directions from a given input file previously prepared; then it assigns these directions to every quadrature point of the whole mesh. This happens at the beginning of the first increment, and before any stress or elasticity tensor calculation takes place. An excerpt of the corresponding UMAT subroutine is:

```
if (flag.EQ.1) then
 if (KINC.EQ.1) then
  IPCOORD(1:KNIP,1)=STATEV(1:KNIP)
  IPCOORD(1:KNIP,2)=STATEV((KNIP+1):(2*KNIP))
  IPCOORD(1:KNIP,3)=STATEV((2*KNIP+1):(3*KNIP))
```

```
 colu = (1+((NOEL-1)*8))+(NPT-1)
 FIBRES(:,colu)=STATEV
 COORDOUT=STATEV
 deleig = 0.0
end if
...
```

Whereby flag.EQ.1 ensures that what follows is applied at the start of every increment; KINC.EQ.1 specialises instructions to the first increment only; STATEV is a variable prepared in and shared from user subroutine SDVINI, which contains the set of initial 184 unit vector directions of the fibres; FIBRES is a local variable created with a save attribute, for STATEV does not keep updated values of the fibre orientations in between increments; COORDOUT is also a local variable and transfers the updated orientation of fibres to an output file named IVARIA; finally, colu simply calculates the column index of FIBRES array associated to current element, whereas deleig stores the anisotropy parameter $|A_1 - A_3|$ and also transfers it to an output file named A1A3AN*.txt.

At the end of the first increment, each element has undergone its own deformation; but, as no fibre orientation $\mathbf{r}_i$ has taken place thus far, there is no apparent remodelling yet. This is visible when, in the Results section, the plot of $|A_1 - A_3|$ corresponding to the first increment is equal to zero for all of the selected elements of the mesh.

At the start of the second increment, each element has its own right-Cauchy Green (isochoric) tensor $\overline{\mathbf{C}}$, so a subroutine in charge of calculating $|A_1 - A_3|$ and then another one for updating $\mathbf{r}_i$ are called. The updated fibre orientations they produce are used to calculate stresses and elasticity tensors specific to the current quadrature point. An excerpt of the relevant instructions is set out below:

```
if (KINC.GE.2) then
 colu = (1+((NOEL-1)*8))+(NPT-1)
 STATEVx = FIBRES(:,colu)
 call calculate_Aeig(STATEVx,WEIGHTS,deleig)
 Adelta = 0.1 ! 0.0 < Adelta < 1.0
 call calculate_int_var(FG,DTIME,STATEVx,C,deleig, &
                         Adelta,rnPlusOne,NOEL,NPT,KINC)
 IPCOORD(1:KNIP,1)=STATEVx(1:KNIP)
 IPCOORD(1:KNIP,2)=STATEVx((KNIP+1):(2*KNIP))
 IPCOORD(1:KNIP,3)=STATEVx((2*KNIP+1):(3*KNIP))
 COORDOUT=STATEVx
 FIBRES(:,colu) = STATEVx
end if
```

Here subroutines calculate_Aeig and calculate_int_var compute $|A_1 - A_3|$ and the updated orientations $\mathbf{r}_i$, respectively. The parameter A_Δ is one from the re-

modelling model, and is part of the variation during the screening study. Other remodelling parameters of said study, namely t^* and Δt, are typed into the body of calculate_int_var subroutine.

Given their central role in the generation of results specific to this work, we set out next the abbreviated contents of subroutine calculate_Aeig first, which implements calculation of the structural tensor **A** from Equation (3.27).

```
subroutine calculate_Aeig(STATEVx,weights,deleig)
C INPUTS:
C STATEVx: set of integration directions
C OUTPUTS:
C deleig: A1-A3 (max-min eigenvalues of structural matrix A)
...
 newcoord(1:KNIP,1)=STATEVx(1:KNIP)
 newcoord(1:KNIP,2)=STATEVx((KNIP+1):(2*KNIP))
 newcoord(1:KNIP,3)=STATEVx((2*KNIP+1):(3*KNIP))
 Atot = 0.0
 absolErr = 1.0e-09

 do i=1,KNIP
  coordsCol(1:3,1) = newcoord(i,1:3)
  coordsRow(1,1:3) = newcoord(i,1:3)
  Adum = matmul(coordsCol,coordsRow)
  Atot = Atot + weights(i)*Adum
 end do

 A = Atot
 call Jacobi(A,x,absolErr,3)
 A1=A(1,1)
 A2=A(2,2)
 A3=A(3,3)
 deleig=abs(max(A1,A2,A3)-min(A1,A2,A3))
end subroutine
```

In the above we notice that Fortran subroutine Jacobi was used to calculate eigenvalues[2] of matrix **A**, so that the criterion in Equation (3.28) can be applied.

The summarised contents of subroutine calculate_int_var are as follows:

```
subroutine calculate_int_var(dfgrd,DTIME,STATEVx, &
 & C,deleig,Adelta,rnPlusOne,NOEL,NPT,KINC)
C INPUTS:
C STATEVx: set of available integration directions
```

---

[2]subroutine taken from https://ww2.odu.edu/ agodunov/computing/programs/

```
C OUTPUTS:
C STATEVx: set of updated integration directions
...
 coorLam(1:KNIP,1)=STATEVx(1:KNIP)
 coorLam(1:KNIP,2)=STATEVx((KNIP+1):(2*KNIP))
 coorLam(1:KNIP,3)=STATEVx((2*KNIP+1):(3*KNIP))

 do i=1,KNIP
  rncol(1:3,1)=coorLam(i,1:3)
  rnrow(1,1:3)=coorLam(i,1:3)
  rnLam(1:3,1)=coorLam(i,1:3)
  g1 = It-matmul(rncol,rnrow)
  g2 = matmul(Ciso,rncol)
  g = matmul(g1,g2)
  t = matmul(dfgrd,rncol)
  trow(1,1:3) = t(1:3,1)
  str = sqrt(dot_product(t(:,1),t(:,1)))
  if (str.le.strc) then
   factor = 0.0
  else
   if (abs(deleig)/Adelta.LE.1.0) then
    factor = (1/tstar)*(1-(abs(Adelta-deleig)/(tstar*Adelta)))
   else
    factor = 0.0
   end if
  end if
  rn1tilde = rncol + DTIME*factor*g*timeFactor
  normrn1tilde = sqrt(dot_product(rn1tilde(:,1),rn1tilde(:,1)))
  if (normrn1tilde.gt.1.0E-6) then
   rncol = rn1tilde/normrn1tilde
  end if
  rnPlusOne(i,1:3)=rncol(1:3,1)
 end do
 STATEVx(1:KNIP)               = rnPlusOne(1:KNIP,1)
 STATEVx((KNIP+1):(2*KNIP))    = rnPlusOne(1:KNIP,2)
 STATEVx((2*KNIP+1):(3*KNIP))  = rnPlusOne(1:KNIP,3)
 return
end subroutine calculate_int_var
```

In the subroutine above we notice that remodelling parameter Δt is incorporated as the product of variable DTIME, which is internal to Abaqus™ and measures the size of the load increment, and a local variable timeFactor, which can be set by the user. As the value DTIME is out of full control on part of the user, there is difficulty in establishing a direct relationship between the value of the product DTIME*timeFactor, and that actually given to Δt in the solution of a

semi-analytical model, as the one presented in the Results section.

The approach so far exposed, in particular that regarding the consideration of evolving fibre orientations by using a static array FIBRES, worked well for coarse meshes up to about 3200 elements. But, when attempting to run this UMAT subroutine using the 68290-elements mesh, Abaqus™ did not allow using FIBRES, for it was beyond the size limit for static arrays. This array was incorporated because, for some reason, the reserved variable STATEV, although updated within UMAT subroutine, it loses its value once UMAT returns control; when called back for the next iteration on a quadrature point, STATEV only keeps the value assigned at the beginning of the analysis through the user subroutine SDVINI.

Furthermore, turning FIBRES to be an allocatable (dynamic) array, along with the save attribute, did not let deallocation of memory once UMAT finished its calculations on a quadrature point. Here, once, again, Abaqus™, to the last of our attempts before preparing this document, did not let continue the analysis under that condition.

We consider, for a future development, creating a local variable within UMAT that reads the updated fibre orientations, and then using a COMMON-BLOCK to pass it on to SDVINI subroutine as a shared variable. The body of this subroutine can then contain some conditional that makes STATEV read the shared variable only at the start of increments two and beyond.

$$4$$

Results

4.1 Semi-Analytic Solution

Here we consider the formulation of a case that is relatively simple to model and easy to test experimentally: the uniaxial, laterally unconstrained tension test. Its solution is not strictly analytic in the sense that one application of a nonlinear approximate solver is needed for the calculation of output variables. However, the solution corresponds to a unique material element, so it can be used to benchmark the responses from the analysis using the finite element method, which will be presented later in a separate section.

The domain is a unit cube that is subjected to a prescribed stretch λ on one of its end faces and directed perpendicular to it; we call this direction 11. The opposite end is fixed in this direction, while transversal deformation, i.e. along directions we call 22 and 33, are allowed. The corresponding deformation gradient tensor is given by Equation (4.1), where λ^* is the stretch in the transversal direction. This quantity and the stress σ_{11} are the unknowns of the problem.

$$\mathbf{F} = \begin{bmatrix} \lambda & 0 & 0 \\ 0 & \lambda^* & 0 \\ 0 & 0 & \lambda^* \end{bmatrix} \tag{4.1}$$

The implementation accepts the explicit use of a volumetric strain energy; the model is then based on the split $\mathbf{S} = \mathbf{S}_{vol} + \mathbf{S}_{iso} + \mathbf{S}_{ani}$ whereupon we apply the relationship $\sigma = J^{-1}\mathbf{F}\mathbf{S}\mathbf{F}^T$.

The nonlinear part of the model, whereby we apply the solver embed in fsolve function of Matlab™, stems from the expression for the 22 direction of stress: the left-hand side is just $\sigma_{22} = 0$, whereas the right-hand side is cast in terms of the lateral stretch λ^*; this constitutes a nonlinear equation on λ^*.

The specific expressions for the stress contributions are those for $\mathbf{S}_{vol}$, $\mathbf{S}_{iso}$ and

$\mathbf{S}_{ani}$, which are then transformed into their Cauchy stress counterparts; they follow Equations (3.15) and (3.13) for the computation of $\boldsymbol{\sigma}_{vol}$; Equations (3.15) and (3.5), for $\boldsymbol{\sigma}_{iso}$; and Equations (3.19), (3.7) and (3.8) for $\boldsymbol{\sigma}_{ani}$.

The remodelling effects are incorporated by an update of the set of fibre orientations $\mathbf{r}_i$ after each converged iterative solution of the nonlinear problem for λ^*. In addition, our implementation also allows for keeping the prescribed stretch λ applied to the material volume, and compute the stress and the $|A_1 - A_3|$ response as time evolves further. As earlier discussed, this is a measure of the extent of gained anisotropy.

To account for soft tissues being almost incompressible, we fix the value of the input variable from Abaqus™ .inp file that controls parameter κ in Equation (3.4) so that it is sufficiently large. We do not comment out this expression from UMAT subroutine, just so we can consider the influence of volumetric strain energy in a future study.

In what follows, we consider responses for Neo-Hookean isotropic; for exponential- and WLC model without remodelling; and for exponential- and WLC model with remodelling. For all of them, we consider two sets of material parameters, as indicated in Table 4.1. These come from the values given to typical medial and adventitia layers of the arterial tube in the work of Alastrue et al. [2]; as indicated in Table 4.1, these will be simply regarded as M-set and A-set of material parameter values henceforth.

Case	Parameter	M-set value	A-set value
Neo-Hookean	μ	1.268	7.560
Exponential	k_1	17.040	58.902
	k_2	3.778	20.220
WLC	B	1.019	2.334
	r_0	1.045	0.414
	L	1.477	0.554

Table 4.1: Sets "M" and "A" of material properties used with the semi-analytic solution to the uniaxial tension problem.

As for the remodelling parameters, we considered the scheme shown in Figure 4.1 for the study of their effect. In it, we first evaluate the combination of values for a *reference point* in what would be a space of variables $[A_\Delta,\ t^*,\ \Delta t]$; then to asses the effect of a change in A_Δ, t^* and Δt, respectively, we apply the set of parameter values corresponding to the points *variation of A_Δ*, *variation of t^** and *variation of Δt*. For each case (exponential and WLC material models with material sets A and M) we produced four plots, whose arrangement is also shown in Figure 4.1.
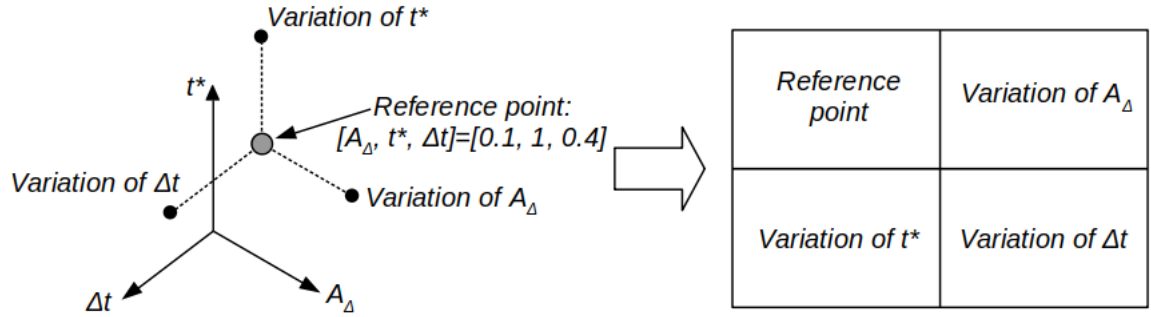
Figure 4.1: Assignment of remodelling parameter values to the study of uniaxial tension case using a semi-analytical model: scheme for value assignation (left); arrangement of plots (right).
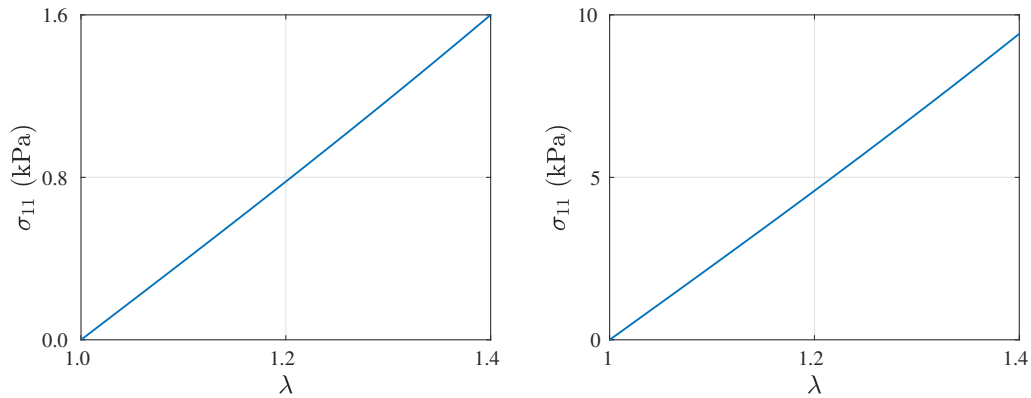

Figure 4.2: Analytic solution to unit cube under uniaxial tension, Neo-Hookean model: M- (left) and A-set (right) material properties.

4.1.1   Neo-Hookean, isotropic model

In principle, there are no limits to the maximum value of the stretch that can be imposed to a material governed by the Neohookean, isotropic strain energy. However, WLC model allows for a maximum stretch along the fibre direction equal to the ratio r_0/L [2]. For the properties in Table 4.1, these maximum values are ≈ 1.35 and ≈ 1.41, for the A- and M-material sets, respectively. From this, we will consider imposed stretches of up to 1.5. for the uniaxial tension case under Neo-Hookean model.

Figure 4.2 shows the evolution of stress with prescribed stretching. Given that the strain energy function depends on the square of the deformation, then the stress-deformation curve is linear. Also, we can see that the A-set material is significantly stiffer than the M-set one.
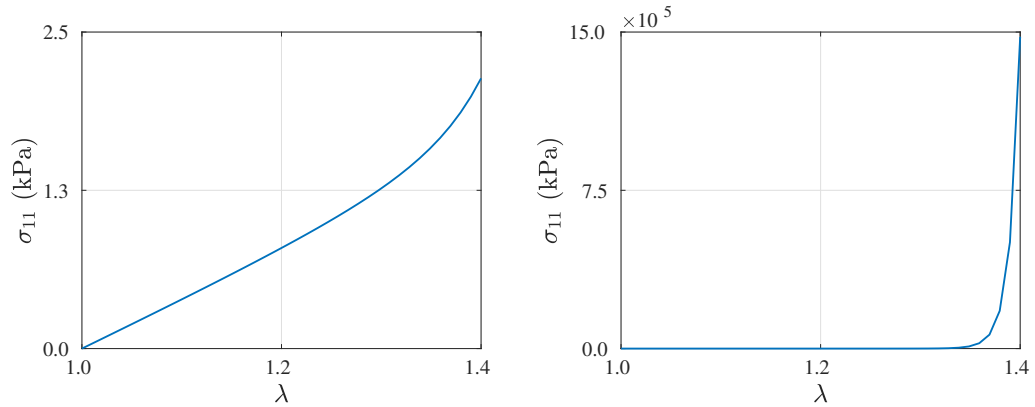
Figure 4.3: Analytic solution to unit cube under uniaxial tension, exponential model: M- (left) and A-set (right) material properties.

4.1.2 Exponential strain energy model

Although there is no reported limit for the value of the stretch that can be prescribed in a uniaxial tension test when using the exponential model, there is a large difference in the stress developed according to the material properties. Figure 4.3 shows the results produced by the exponential strain energy for the fibre, where it is clear that a smaller stretch can be applied when using the A-set material properties, before stress values grow out of proportion. Furthermore, with the A-set properties, almost all of the stiffening of the material takes place at the upper limits of stretching.

When considering the effect of remodelling, we recall that it enters the formulation as an irreversible mechanical process, whereby an internal variable -here the orientation of the fibres- experiences an evolution. The stress response and anisotropy gain that follows such evolution depend on the rate at which external load or prescribed traction is applied.

The time over which the total external action is applied is the product of the -arbitrary- number of increments we split that external action into, and a time increment Δt; this is the time, in arbitrary units, we let the material evolve under the action of any given increment of the external action before the next one is applied. This evolution is analogous to a stress relaxation test on a viscoelastic material.

So, in our example, if $\Delta t = 0.1$ (arbitrary) seconds, and we split the application of external action into 40 increments, then said application takes four (arbitrary) seconds. Clearly, smaller values of Δt represent faster application of external load.

After consideration of Δt, the two parameters that are left to control the remodelling process are t^* and A_Δ The former acts out as a relaxation time, and is

inversely proportional to the factor f_i of equation (3.26); the latter sets a limit to the evolution of fibre orientation $\mathbf{r}_i$: once $|A_1 - A_3|$ equals A_Δ, $f_i = 0$.

Figure 4.4 shows the effect of varying t^*, A_Δ and Δt on the stress σ_{11} and on the parameter $|A_1 - A_3|$; the latter represents the extent to which the material has gained anisotropy ($|A_1 - A_3| = 0$ corresponds to full isotropic condition). The combination [1, 0.1, 0.4] for $[t^*, A_\Delta, \Delta t]$ serves as reference response, and indicates the general trends: stiffening evolves exponentially, and the anisotropy evolves in a way similar to the response to stress relaxation tests in viscoelastic materials; once anisotropy gets to a maximum value, it remains there. A_Δ clearly sets a limit to the anisotropy gain.

Raising A_Δ (top-right panel) brings about a non-uniform gain of anisotropy: up to an applied stretch $\lambda \approx 1.2$ the evolution is as shown in the reference case; but then it continues as though another, independent increase of anisotropy took place. Furthermore, the material stiffens significantly with respect to the reference case.

The increase of t^* defers attainment of maximum anisotropy to $\lambda \approx 1.5$, while also stiffening the material with respect to the results from the reference set of values. No additional or independent process of anisotropy gain takes place. Furthermore, a similar effect is obtained when reducing the time step Δt (bottom right panel), while the material is about as stiff as in the reference case.

The main change exhibited by the exponential model subject to remodelling and with the material properties of the A-set is the much larger stiffening than with M-set properties. This follows the trend shown in Figure 4.3. Meanwhile, Figure 4.5 shows the details of the interaction with fibre remodelling, again with respect to a reference case.

Furthermore, there is no effect in the way the extent of anisotropy evolves. Apparently, with the set of considered values, most of the mechanical stiffness of the composite depends on the stiffness of the fibres rather than on their reorientation.

4.1.3 WLC strain energy model

In this case the maximum stretch applied to the unit cube is the ratio r_0/L. For the M- and A- set material properties, it is $\lambda \approx 1.41$ and $\lambda \approx 1.34$, respectively. For the case without remodelling, the evolution of stress σ_{11} is shown in Figure 4.6.

The gain of stiffness is somewhat more pronounced than that from the exponential model, whereas, just as in the exponential model case, A-set material properties result in a stiffer material.
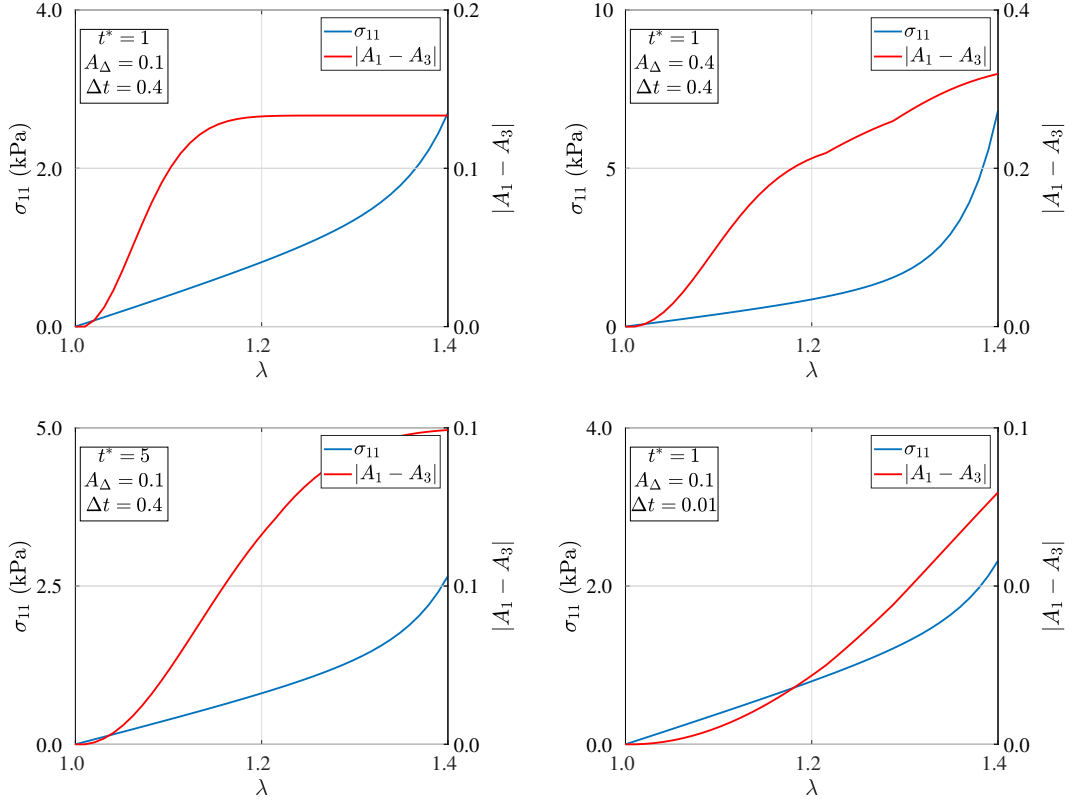
Figure 4.4: Analytic solution to unit cube under uniaxial tension. Exponential model with remodelling and M-set material properties for a series of $[t^*, A_\Delta, \Delta t]$ combinations (see Figure 4.1): reference values (top left), and effect of changing A_Δ (top-right), t^* (bottom left) and Δt (bottom right).

As for the response of the WLC model with the effect of remodelling, Figure 4.7, the reference case (top left panel) shows how the anisotropy indicator $|A_1 - A_3|$ again evolves as though in a viscoelastic material under a stress relaxation test: the fibre orientations reach a plateau whereby the eigenvectors of structural matrix $\mathbf{A}$ are aligned to that of right Cauchy-Green isochoric tensor $\overline{\mathbf{C}}$. Increase of the limiting value A_Δ greatly increases the stiffness, while, as expected, the degree of anisotropy that is gained also increases, though in a non-uniform way. Increase of relaxation time parameter t^* seems to have little effect on the stiffness, but defers attainment of maximum anisotropy to the latter instances of applied stretch λ. And decrease of Δt, which represents a faster application of external load, lowers the stiffness gained by the material and also the degree of anisotropy reached; furthermore, the material does not seem to get to the full extent of anisotropy under the maximum applied stretch.

When we consider the WLC model with remodelling and the A-set material properties, Figure 4.8 shows that the reference case corresponds to a stiffer material than that of the M-set properties. No significant difference is seen in the effect
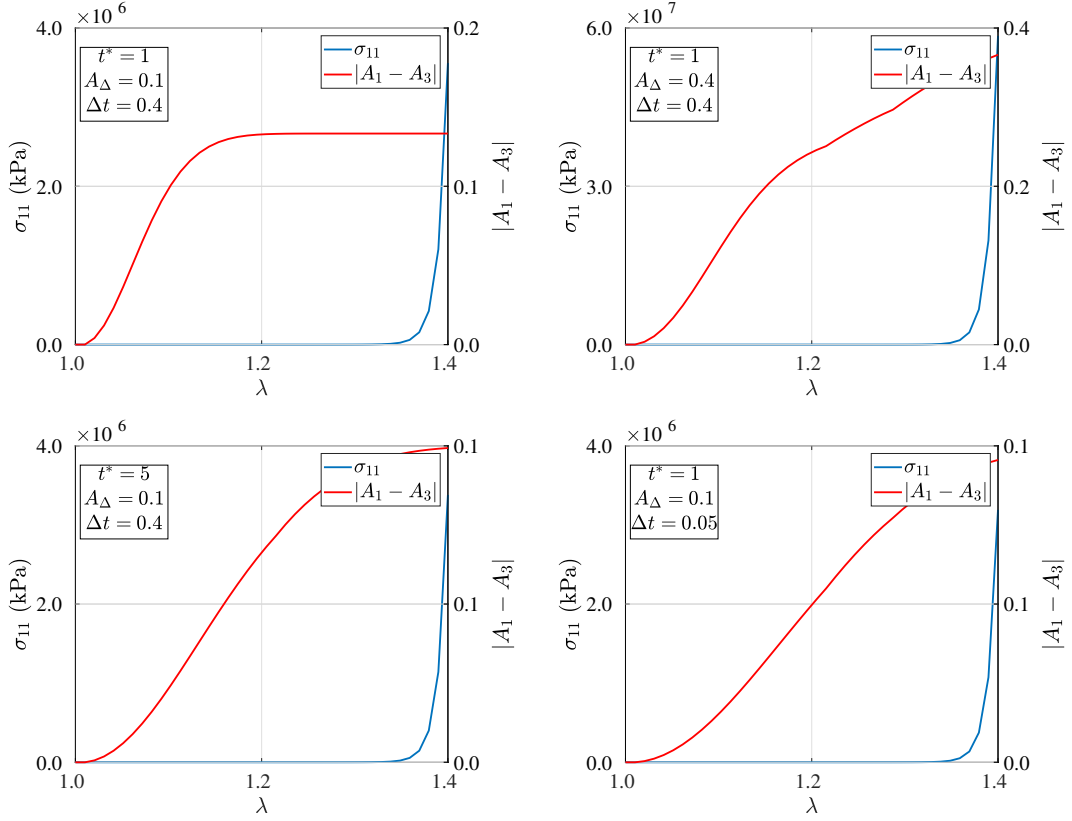
Figure 4.5: Analytic solution to unit cube under uniaxial tension. Exponential model with remodelling and A-set material properties for a series of $[t^*, A_\Delta, \Delta t]$ combinations (see Figure 4.1): reference values (top left), and effect of changing A_Δ (top-right), t^* (bottom left) and Δt (bottom right).

of changing A_Δ, while increasing t^* and decreasing Δt produced a stiffer material than with the M-set properties.

The semi-analytical model also allows visualising the pattern that fibres take on as result of the remodelling action. The initial state is that of an isotropic distribution of the fibres over a unit sphere, whereas the parameter combinations that lead to the highest values of A_Δ lead to the most marked remodelling effects on the pattern of the set of fibres. In this regards, Figure 4.9 shows these two case; the latter corresponds to the WLC model with A-set material properties and remodelling parameters $[t^*, A_\Delta, \Delta t] = [1, 0.4, 0.4]$.

It is interesting to note how the stress and the anisotropy indicator $|A_1 - A_3|$ evolve when we let the material be under the fixed action of the stretch λ once it reaches its prescribed value, as though in a stress relaxation test. As it is a typical feature of the study of viscoelastic materials, the main effect in the response would come from the speed with which the stretch is applied. Here we selected the scenario under WLC model with remodelling and M-set material properties, and two
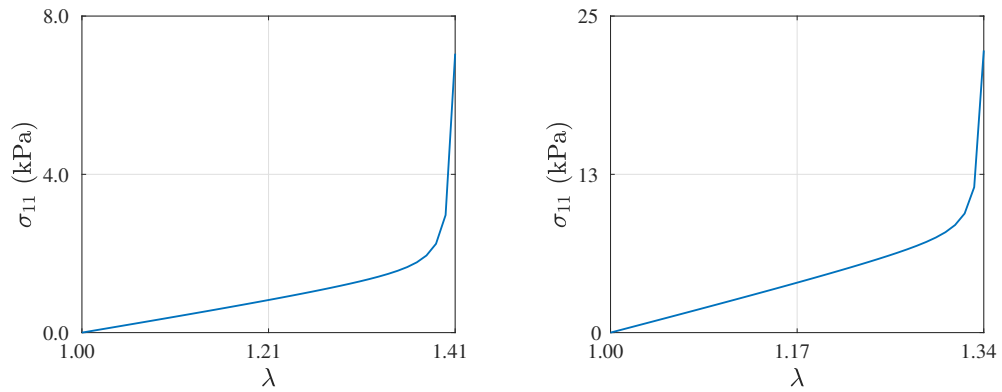
Figure 4.6: Analytic solution to unit cube under uniaxial tension, WLC model model: M- (left) and A-set (right) material properties.
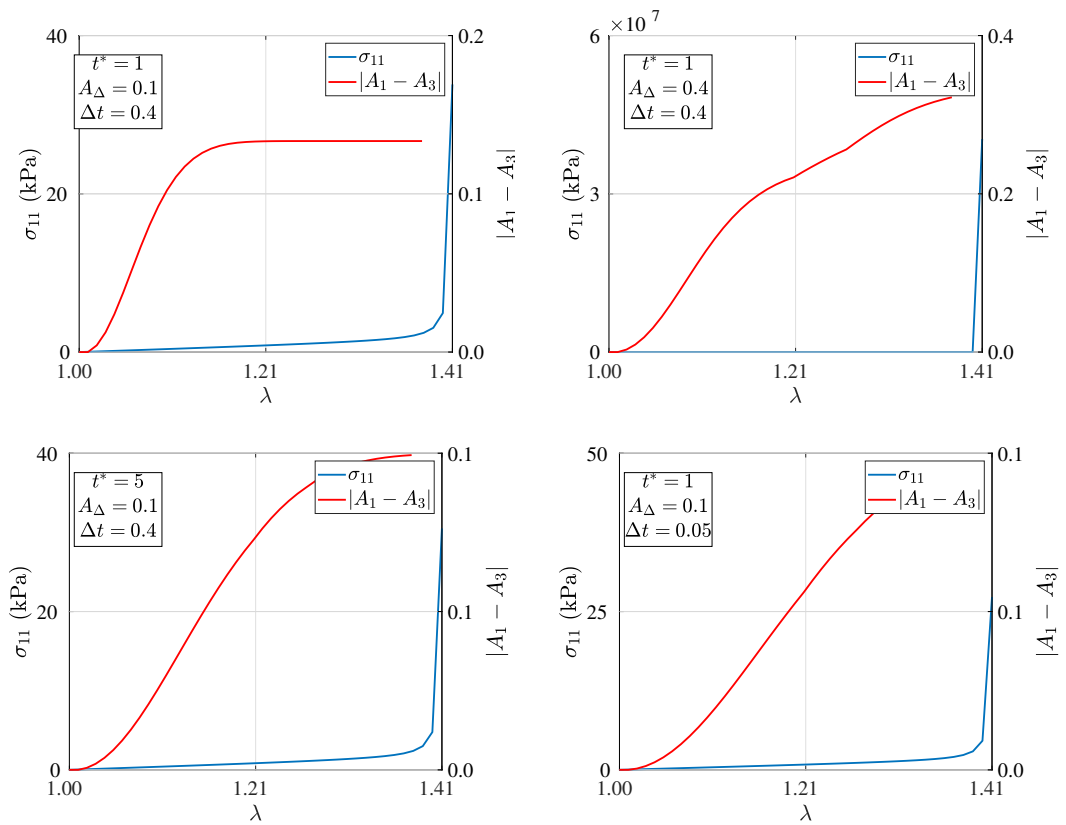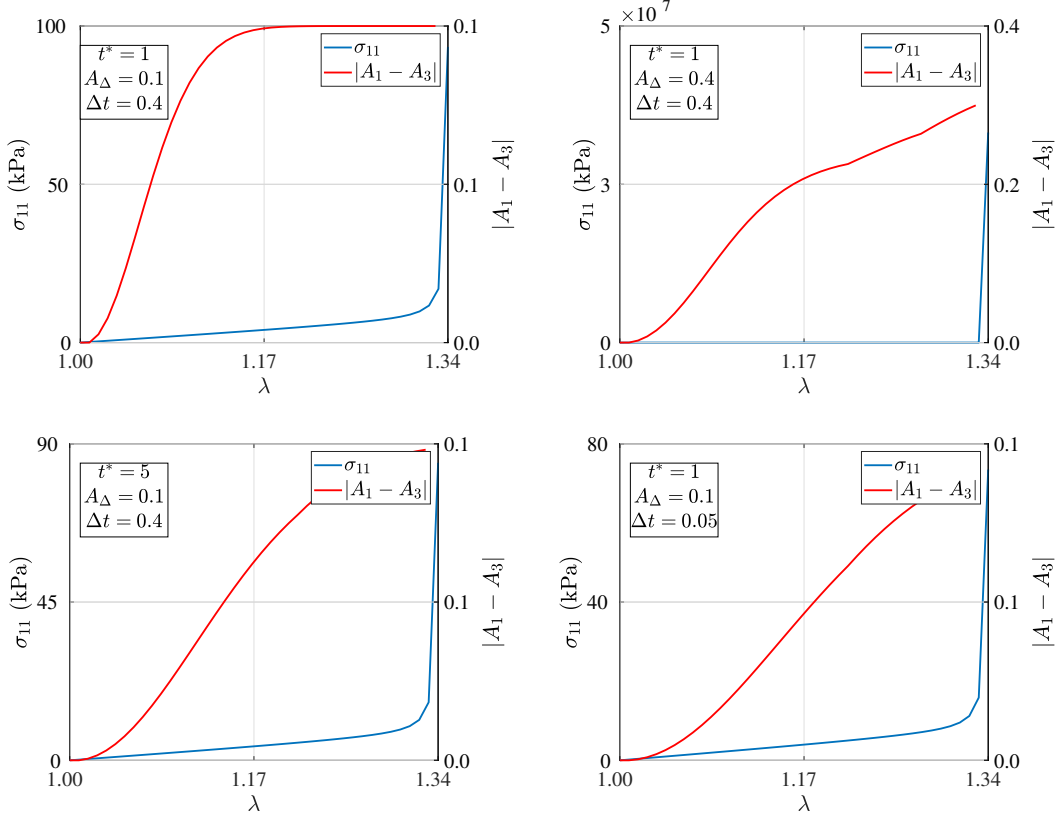

Figure 4.7: Analytic solution to unit cube under uniaxial tension. WLC model with remodelling and M-set material properties for a series of $[t^*, A_\Delta, \Delta t]$ combinations (see Figure 4.1): reference values (top left), and effect of changing A_Δ (top-right), t^* (bottom left) and Δt (bottom right).

Figure 4.8: Analytic solution to unit cube under uniaxial tension. WLC model with remodelling and A-set material properties for a series of $[t^*, A_\Delta, \Delta t]$ combinations (see Figure 4.1): reference values (top left), and effect of changing A_Δ (top-right), t^* (bottom left) and Δt (bottom right).

combination of remodelling parameters, whereby only Δ_t is allowed to change. As earlier mentioned, smaller Δt represents faster application of the external stretch.

In this regards, Figure 4.10, left panel, and comparison with the reference case from Figure 4.7 (top left panel), indicates how the material continues its gain of anisotropy, while the exponential growth of stiffness breaks and resumes following a much shallower trend. We notice that the x axis represents an arbitrary time τ, where it is clear that the time taken to apply the prescribed stretch is smaller as Δt is given a smaller value also.

The right panel of Figure 4.10 shows how a faster application of stretch defers the attainment of the maximum extent of anisotropy beyond λ_{max}; however, from the point of view of arbitrary time τ, this full extent of anisotropy takes less time.

At the point of maximum imposed stretch, the faster application of it produces a less stiff material; however, the stress tends to keep growing, much unlike the slower-application of stretch case, where it remained without further change.
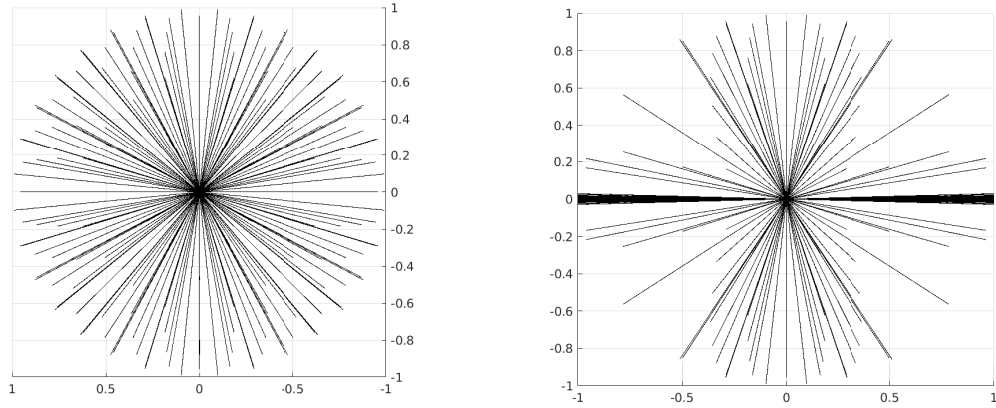
Figure 4.9: Initial, isotropic fibre distribution (left), and distribution after application of a stretch $\lambda \approx 1.34$ to the unit cube (right). WLC model with A-set material properties and remodelling parameters $[t^*,\ A_\Delta,\ \Delta t] = [1,\ 0.4,\ 0.4]$.
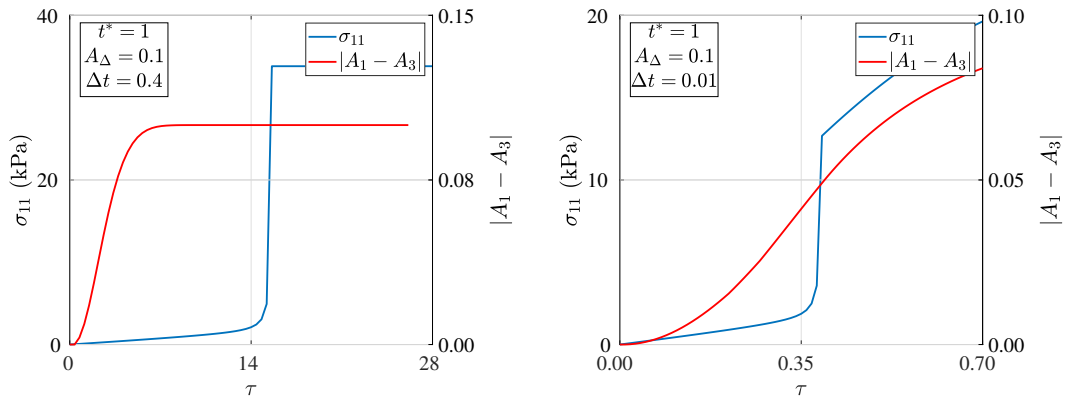

Figure 4.10: Analytic solution to unit cube under uniaxial tension, WLC model and M-set material properties: imposed $\lambda_{max} \approx 1.41$ is reached at (arbitrary) time $\tau \approx 15$ (left) and $\tau \approx 0.4$ (right), and held fixed at that value from then on.

4.2   Numerical Results

We start by running a simple shear FE simulation to visualise the contributions of this fundamental stress state to what would be a more complex one; this is to complement the results already observed in the semi-analytical solution, which corresponds to a 1D tensile state. Here we considered the exponential- and WLC models with fibre remodelling and used a single combination of material properties and of remodelling parameters.

Then, in the light of the large number of possible combinations given by the material parameters considered in this work, we ran a screening set of runs for the plate with two holes case. The purpose of this study was to identify a combination of material properties and of remodelling parameter values with which the stiffening and the remodelling effects, in addition to their propagation in space, were evident. To that end, we obtained the variation of stress components and of the anisotropy evolution parameter $|A_1 - A_3|$ as one moves away from a hole edge in the direction of the neighbouring hole. Also, the fibre patterning associated to remodelling is here presented.

The holes were used to prescribe a boundary displacement in the form or a radial contraction; the outer borders of the plate had zero prescribed displacement, and the plate was considered to be under plane strain state.

4.2.1   Simple shear test simulation

The simple shear tests was simulated for a 9x9x9 `C3D8H` mesh. The purpose is to visualise the main features of material stiffening and fibre reorientation under this fundamental deformation condition. This can add further insight into the results obtained for the plate with two holes using a coarse mesh, particularly on the vicinity of the hole edge, where a radial displacement is prescribed. There, the stress gradient is large and the stress state itself can also be complex, so a general mesh makes it difficult assessing the factors behind remodelling and stiffening.

The set of material and remodelling properties were selected from the combinations that the screening tests suggested could be more influential in generating a response, as revealed in the next section. The exact values used to produce the figure of this section appear in the corresponding caption.

Figure 4.11 shows the stress and right-Cauchy Green strain components taking place on the plane of shearing, when considering the exponential strain energy model for the fibres. The anisotropy gain parameter $|A_1 - A_3|$ is also shown. As

regards the WLC strain energy model, given that practically the same results were obtained for stress and strain components, we do not repeat them here. In addition, though there is some difference in the value of $|A_1 - A_3|$ (the maximum value is ≈ 0.66 for the WLC model versus ≈ 0.73 for the exponential one), the distribution pattern over the domain is also the same, and thus not repeated either. Furthermore, the right-Cauchy Green components shown in the colour scale follow the notation assigned by Paraview™, whereby $C\_0 = C_{11}$, $C\_2 = C_{22}$ and $C\_8 = C_{33}$.

The material parameters applied correspond to those of the A-set shown in Table 4.1, while the caption indicates those used in the remodelling expressions.

A salient feature of the result is the localisation of the fibre reorientation on the left edge of the top surface, where displacement was prescribed. Furthermore, the relative magnitudes of the stress and strain components are similar to each other. So, regions of a domain subjected to prescribed shearing may not favour one specific direction for reorientation. In the remodelling model used in this work, these are dictated by the eigenvectors of right-Cauchy Green tensor. The off diagonal components of this strain tensor are almost zero in comparison.
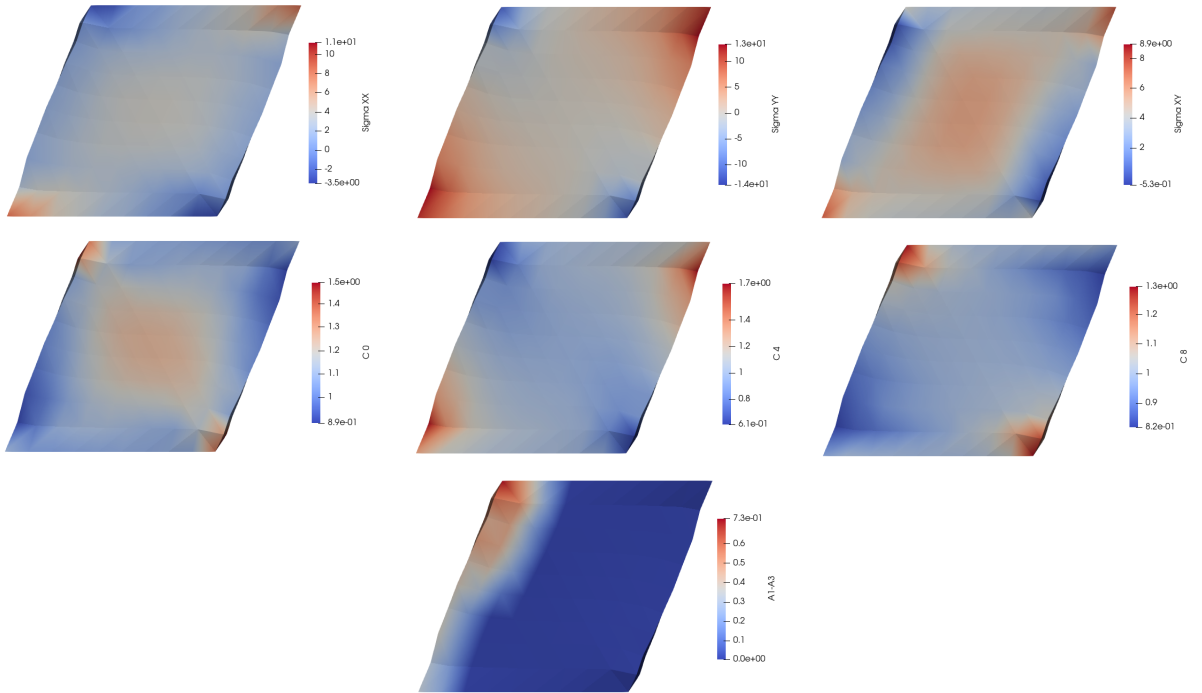

Figure 4.11: Stress (top row, in kPa) and right-Cauchy Green (middle row) components, and anisotropy gain parameter $|A_1 - A_3|$ for the exponential model with remodelling. Exponential strain energy parameters for the A-set material properties; remodelling parameters $[A_\Delta,\ t^*,\ \Delta t] = [0.8,\ 0.1,\ 0.5]$

.

4.2.2 Screening of Material Parameters

The plate with two holes represents a region in the connective tissue whereby the interaction of two neighbouring cells, typically fibroblasts, emerges as a result of a prescribed radial contraction. Given the number of combinations that are possible with the material models here considered and the fact that there is a complex stress state in the vicinity of hole edges, we ran FE simulations of the plate with two holes case with a relatively coarse mesh. In this way, we intended seeing only general trends at least to the point of being able to identify interesting combinations of material parameters, while keeping calculation times reasonably short.

Here, we plotted the variation of stress components σ_{11}, σ_{22} and $\sigma12$, and that of the anisotropy evolution parameter $|A_1 - A_3|$ as one moves from the edge of the hole to a place in the middle of the two hole centres. For that, we selected the aforementioned values at quadrature point #1, as assigned internally by Abaqus™, for a set of 13 elements located in between the holes of the plate, as indicated in Figure 4.12.
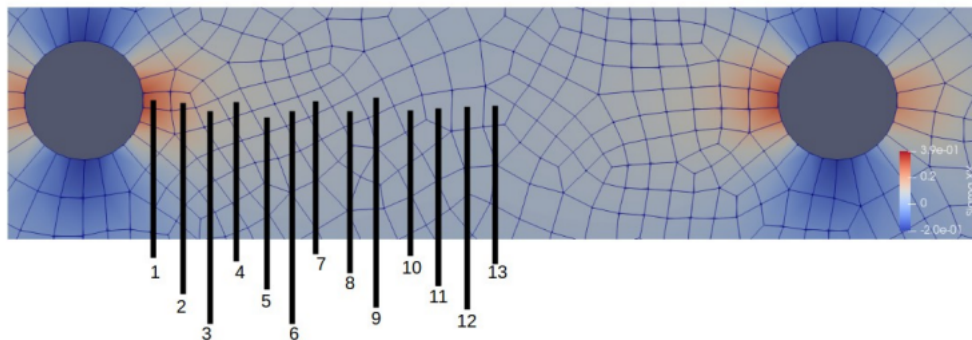

Figure 4.12: Elements whose quadrature point #1 provided the values of σ_{11}, σ_{22} and $|A_1 - A_3|$ for the parameter screening study. Only a fraction of the whole plate is shown here

To formulate the combination of material properties to screen over with the FE simulations, we proposed the array of values for exponential, WLC and re-modelling models shown in Tables 4.3, 4.2 and 4.4, respectively. Then, to screen over the parameters of the WLC- and exponential model, we fixed the remodelling parameters at one specific combination; these are shown in the captions of the corresponding figures. To screen over the remodelling parameters, we fixed first the WLC- and then the exponential model parameters at the values for the A-set material properties.

The values for the parameters of the fibre-strain energy models were taken so as to span those reported by [2] for the media and adventitia layers of the arterial tube. Given that these values stem from actual experiments, they may not be arbitrarily chosen [73]. Additionally, the variation of the values reported for these

Parameter	value 1	value 2	value 3
B (kPa)	1.0	5.0	2.5
r_0 (mm)	0.4	0.8	1.2
L (mm)	0.5	1.0	1.5

Table 4.2: Values of WLC-model properties for parameter screening study. Remodelling parameters held constant at $A_\Delta = 0.4$, $\Delta t = 0.5$ and $t^* = 5$.

Parameter	value 1	value 2
k_1 (kPa)	15	60
k_2 (mm)	3	22

Table 4.3: Values of exponential model properties for parameter screening study. Remodelling parameters held constant at $A_\Delta = 0.4$, $\Delta t = 0.5$ and $t^* = 5$.

curve-fitted properties can be significant.

Convergence of simulations in a reasonable number of increments and iterations within them proved to be very sensitive to the value for radial, prescribed contraction of the holes. For instance, small values of the Neo-Hookean strain energy parameter C_{10} led to convergence problems and forced to using small contractions, while being overly conservative in this sense also led to fast converging simulations, but with very little changes in regards of stiffness or fibre remodelling. Here we used a radial contraction of about 20% the original radius of the hole.

Exponential- and WLC parameters.

Here we fixed the remodelling parameters at $[A_\Delta, \Delta t, t^*] = [0.4, 0.5, 5]$ and run all 27 possible combinations from Table 4.2 and the four from 4.3. The results indicate no visible difference in their effect on the way the tension components σ_{11} and σ_{22} evolve as increments of the applied prescribed radial contraction take place. No difference is seen in the evolution of the anisotropy gain parameter $|A_1 - A - 3|$ either.

Figure 4.13 shows the main aspects of the evolution of σ_{11} and σ_{22}, while Figure 4.14 does that for the evolution of $|A_1 - A_3|$, for a selected combination of WLC-model parameter values indicated in the caption.

Parameter	value 1	value 2	value 3
A_Δ	0.1	0.4	0.8
t^*	0.1	5.0	20.0
Δt	0.1	0.5	1

Table 4.4: Values of remodelling model properties for parameter screening study. WLC properties held constant at $B = 2.334$ kPa, $r_0 = 0.414$ mm and $L = 0.554$ mm; exponential model properties held constant at $k_1 = 58.902$ kPa, $k_2 = 20.220$.
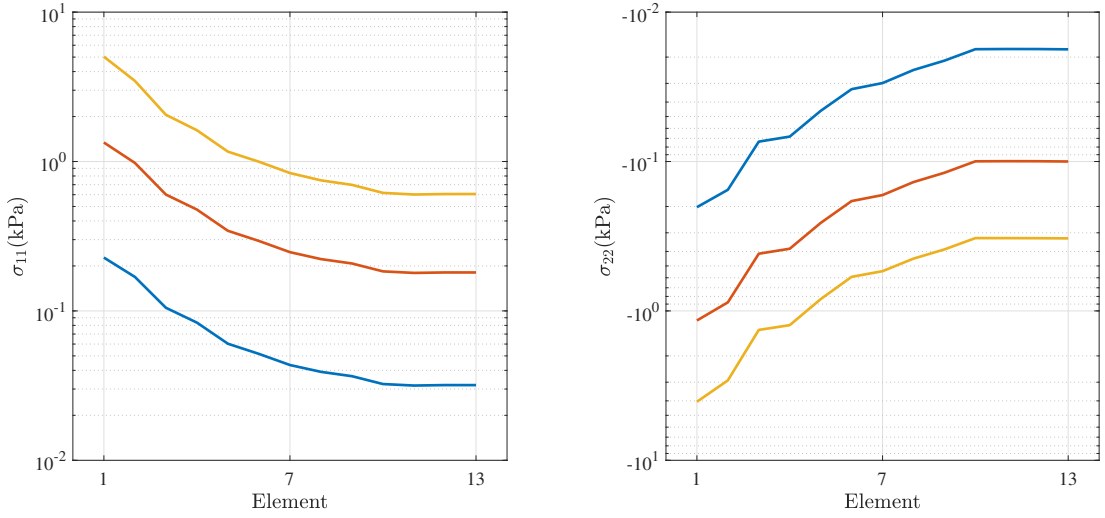

Figure 4.13: Evolution of σ_{11} and σ_{22} for WLC-model with parameters $B = 1.0$ kPa, $r_0 = 0.8$ mm and $L = 1.5$ mm and remodelling parameters $A_\Delta = 0.1$, $\Delta t = 1.0$ and $t^* = 5$. Values taken from data in Table 4.2. Results for first (blue), intermediate (orange) and last (yellow) increment.

For the exponential model case, the corresponding results are shown in Figures 4.15 and 4.16, respectively, again for a selected combination of the exponential model parameters.

In the evolution of $|A_1 - A_3|$ the first increment considers the starting condition of the set of fibres, which represent an isotropic distribution; hence, the anisotropy evolution parameter $|A_1 - A_3|$ is zero.

As regards σ_{22}, the series that are placed lower in the vertical direction represent negative values further away from zero.

The lack of more significant differences in stiffening, mainly in the values of σ_{11}, could be due to a too small radial contraction being applied. However, slight differences can be seen in the way this stiffness is gained as increments evolve, and
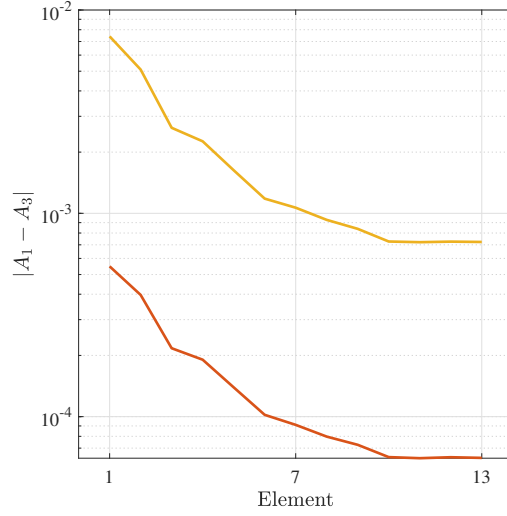
Figure 4.14: Evolution of $|A_1 - A_3|$ for WLC-model with parameters $B = 1.0$ kPa, $r_0 = 0.8$ mm and $L = 1.5$ mm and remodelling parameters $A_\Delta = 0.1$, $\Delta t = 1.0$ and $t^* = 5$. Values taken from data in Table 4.2. Results for intermediate (orange) and last (yellow) increment.

in how much stresses drop when going further away from the hole edge towards the plate centre.

Remodelling parameters and WLC model

The screening over parameters of remodelling revealed significant changes on some regions of the range of values proposed in Table 4.4. Figure 4.17 shows a comparison of σ_{11}, σ_{22}, σ_{12} and $|A_3 - A_1|$, respectively. Captions indicate the corresponding values of remodelling parameters.

Stress component σ_{11} is the highest in value, and this happens at the element lying on the edge of the hole; but stress gradients are also steeper here, so there are significant differences among the stress values of the eight quadrature points of the element, particularly in the last increment, where the totality of the prescribed radial contraction has already been applied. In the specific case of Figure 4.17, $\sigma_{11} \approx 5.55$ kPa corresponds to the quadrature point #1, while that from point #4 of the same element is ≈ 23.84 kPa. So too happens with other stress components considered in this parameter screening study.

Although these differences among stress values do not change the general evolution trends along the direction connecting the centres of the plate holes, it constitutes a caveat in the interpretation of maximum attainable stress values due to the combination of fibre reinforcement and anisotropy.
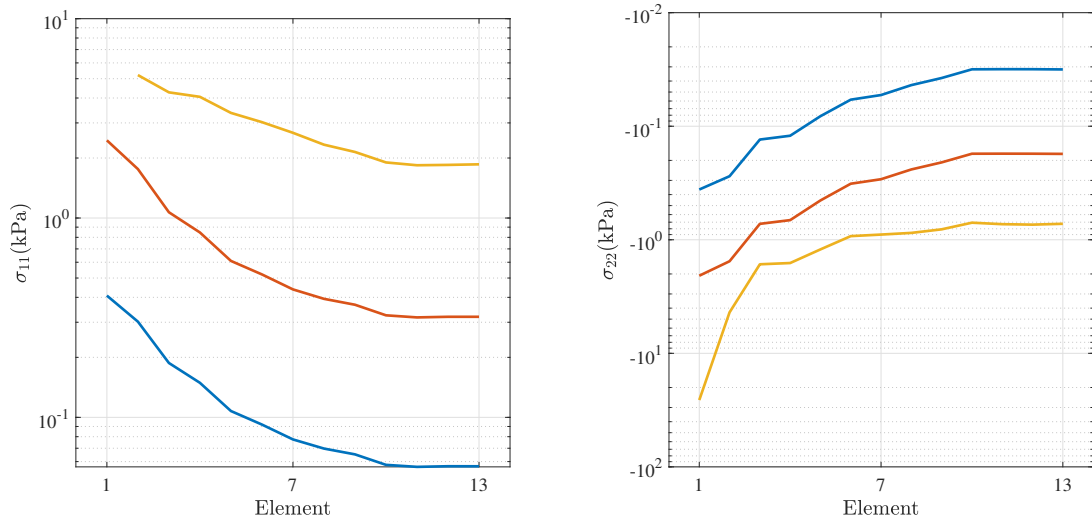
Figure 4.15: Evolution of σ_{11} and σ_{22} for exponential model with parameters $k_1B = 15$ kPa and $k_2 = 22$, and remodelling parameters $A_\Delta = 0.4$, $\Delta t = 0.5$ and $t^* = 5$. Values taken from data in Table 4.3. Results for first (blue), intermediate (orange) and last (yellow) increment.

The evolution of the anisotropy parameter $|A_1 - A_3|$ is intended to represent the traction transfer in between cells embedded in connective tissue. However, its value does not tell anything specific as regards the pattern taken on by the set of fibres as prescribed radial traction is applied. It actually depends on the combined state of stress and, particularly, of deformation, for the eigenvalues of the right Cauchy-Green tensor $\overline{\mathbf{C}}$ determine the orientations the remodelling fibres tend to.

Here, the bottom row of Figure 4.17 provides a picture of the pattern adopted by fibres at the last increment, in quadrature point #1 of the element on the hole edge.

The case corresponding to the right column in Figure 4.17 produces the stress pattern shown by Figure 4.19. A logarithm scale has been used to highlight the relative relevance of stress components in orders of magnitude, particularly given the fact that their values decrease in exponential manner as one moves away from the hole edges.

As expected, stress component σ_{11} prevails in the region in between the holes, while σ_{22} does above and below them. Interestingly, their maximum values are relatively close to each other.
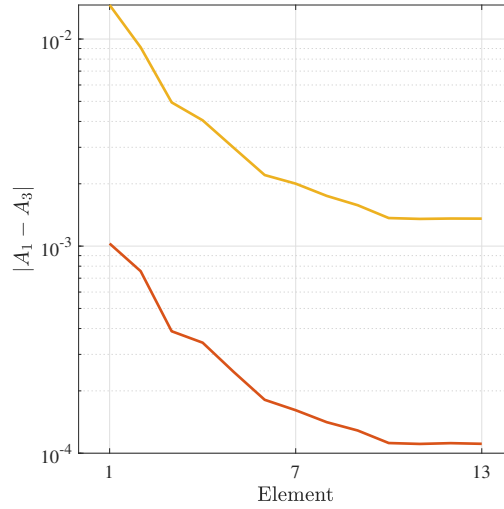
Figure 4.16: Evolution of $|A_1 - A_3|$ for exponential-model with parameters $k_1 = 15$ kPa and $k_2 = 22$, and remodelling parameters $A_\Delta = 0.4$, $\Delta t = 0.5$ and $t^* = 5$. Values taken from data in Table 4.3. Results for intermediate (orange) and last (yellow) increment.

Remodelling parameters and exponential model

As with the WLC model, the effect of varying remodelling parameters was also significant when using the exponential strain energy for the fibres. Here, Figure 4.18 comes from the screening study guided by data in Table 4.4 and, as in the previous section, they refer to the evolution of σ_{11}, σ_{22} and $|A_1 - A_3|$ when moving from the hole edge to the plate centre.

Similar to the evolution of the parameter $|A_1 - A_3|$ using the WLC fibre strain energy, there are also combinations of remodelling parameters at which the intended force transfer mechanism in between cells seems to be enhanced.

The stress distribution for the case corresponding to the right column in Figure 4.18 is displayed in Figure 4.20. Analogous to the WLC case, σ_{11} predominates along the line in between the holes, whereas so do σ_{22} on above and below them. Also, their magnitudes are relatively close.
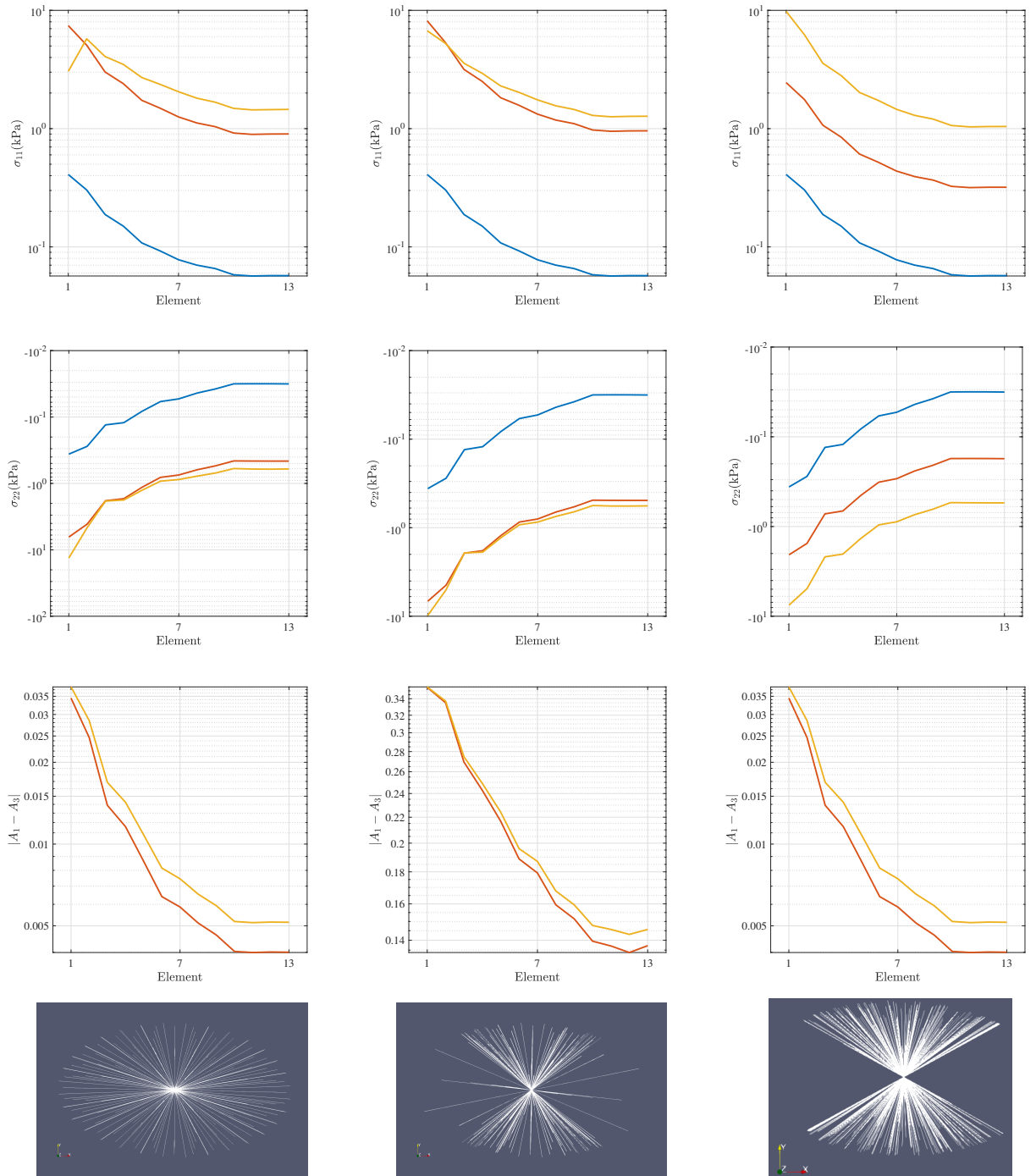
Figure 4.17: Evolution of σ_{11}, σ_{22}, $|A_1 - A_3|$ and of fibre pattern (top to bottom rows) for values of remodelling parameters $[A_\Delta, t^*, \Delta t] = [0.1, 0.1, 0.1]$ (left); $[0.4, 0.1, 0.1]$ (middle); and $[0.8, 0.5, 1]$ (right). WLC model for fibre strain energy. Results for first (blue), intermediate (orange) and last (yellow) increment.
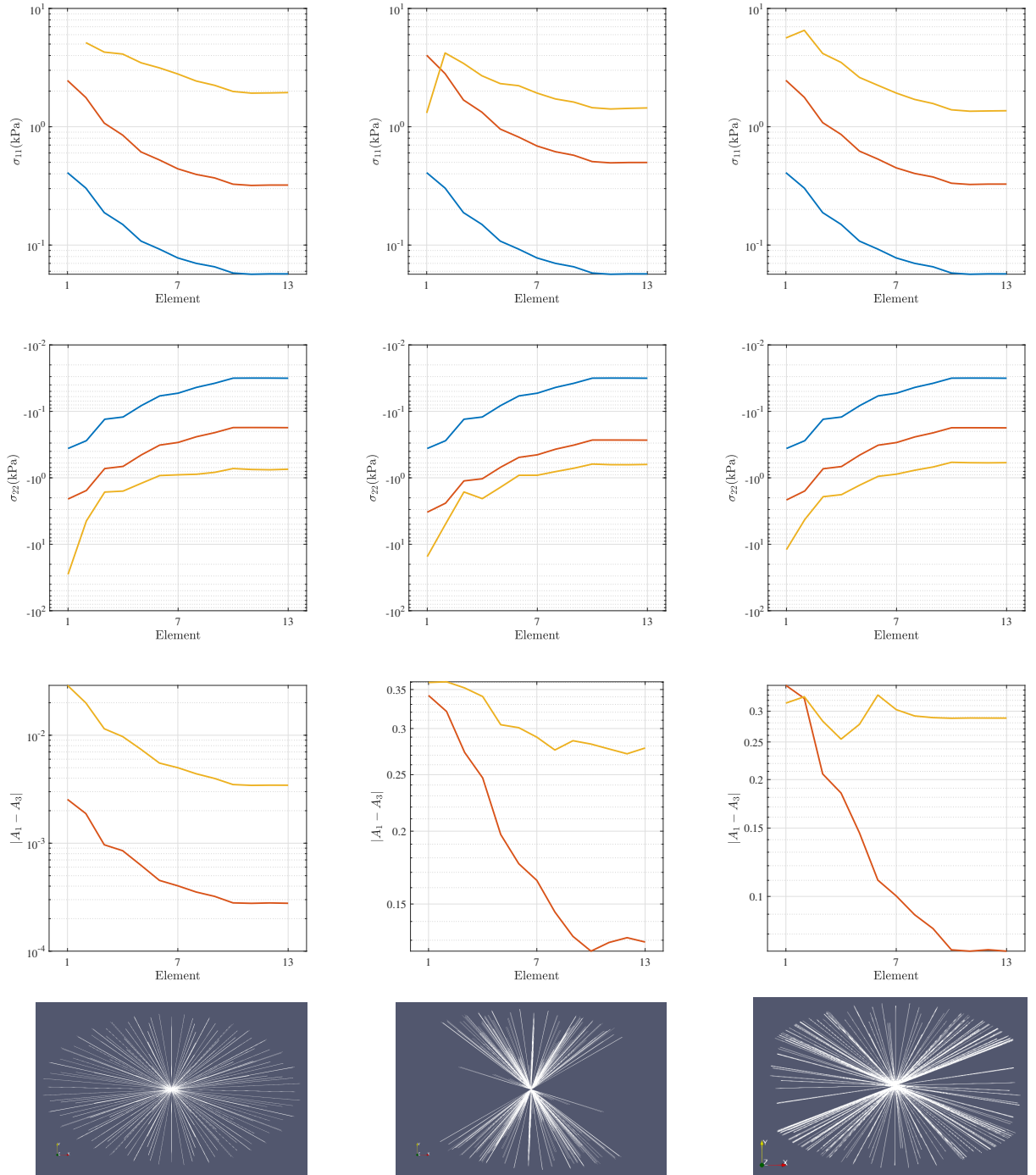
Figure 4.18: Evolution of σ_{11}, σ_{22}, $|A_1 - A_3|$ and of fibre patterns (top to bottom row) for values of remodelling parameters $[A_\Delta, \ t^*, \ \Delta t]$=$[0.1, 0.1, 0.1]$ (left); $[0.4, 0.1, 0.1]$ (middle); and $[0.8, 0.5, 1]$ (right). Exponential model for fibre strain energy. Results for first (blue), intermediate (orange) and last (yellow) increment.

Figure 4.19: Stress distribution in the region in between plate holes, corresponding to the parameters applied to the right column case of Figure 4.17: σ_{11} (top), σ_{22} (bottom)
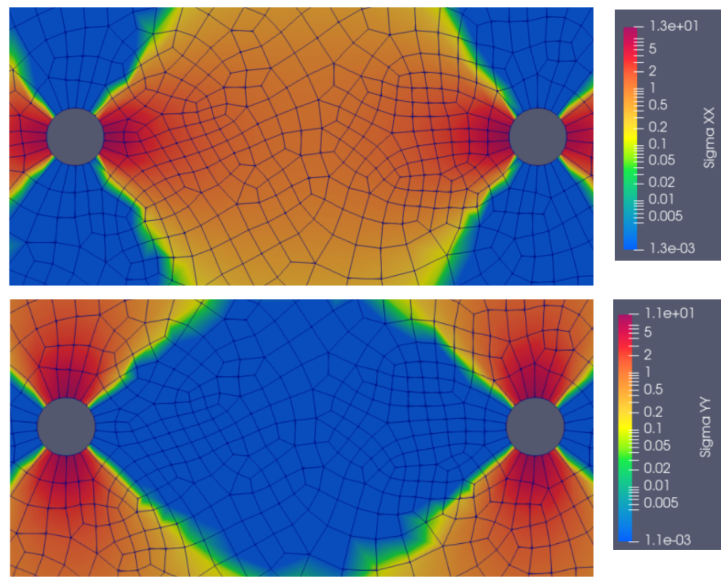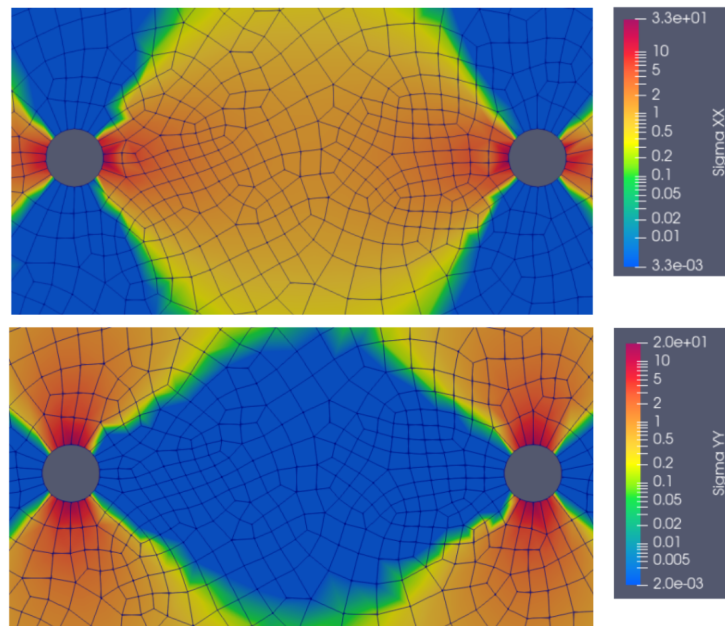

Figure 4.20: Stress distribution in the region in between plate holes, corresponding to the parameters applied to the right column case of Figure 4.18: σ_{11} (kPa, top), σ_{22} (kPa, bottom).

5

Discussion

In the context of fibre remodelling and the transmission of force between cells embed in a wide variety of connective tissues, the phenomenon has long been identified, as reported in the work of Wang et al. [74]. The extent to which such transmission takes place, in relation to the size of the cells, typically fibroblasts, the realisation that collagen fibres are way stiffer than elastin ones, and the role of fibre orientation in response to applied deformation, led to the generation of models aimed at reproducing this scenario.

The results from the semi-analytic model proposed in this work, assign a significant part of the stiffness to the properties of the reinforcing fibres, particularly at large stretches and for the exponential material model. Here, at relatively small values of parameter k_2, results indicate that the extent of fibre orientation is in fact associated to larger stiffness of the whole tissue; whereas larger values for this same parameter renders the participation of fibre reorientation in the generation of a stiffer material almost ineffectual.

In the case of WLC material model, the remodelling parameter A_Δ is the one that associates fibre reorientation with material stiffening to an extent that surpasses that owed to the effect of WLC material parameters alone.

In this sense, we may understand the stiffening not associated to fibre reorientation as strain hardening of an isotropic surface matrix. More so if we consider that the set of fibre directions that are input to our models is indeed uniformly distributed over a sphere surface. Some works share this view of the situation: Winer et al. [78] indicates that nonlinear strain hardening isotropic gels promote cell elongation, which is attributed to force transmission in between cells themselves, particularly at small values of stiffness of that isotropic matrix. This situation could be analogous to our results using the exponential model for the fibres and relatively large values of parameter k_1. In this case of small stretch-small stresses regime, we could say that the fibres of the exponential model, rather than the collagen, would rather represent the role of elastin fibrils.

In a reference to the role of the isotropic matrix stiffness, Leong et al. [44] claim that a higher value promotes interaction between cells, while low stiffness inhibited polymerisation of actin, a molecule that enables mechanical motion and deformation of the cell. The increased interaction, however, was linked to the proximity to the rigid substrate of the culture in which the study was made. In this sense, we may turn to the results from the FE simulation of the simple shear case, in which remodelling was observed close to boundaries of prescribed displacement. Though the work of the same authors suggests that our model could be enhanced towards reproducing their experimental observations, we must bear in mind that remodelling should have taken place along all the prescribed displacement boundaries, and not just in a localised zone. Here, it could argued about some kind localisation phenomenon of the fibre orientation, if we see it as an internal variable associated to irreversible changes. But that is clearly only a speculation, and a thorough revision of the implementation must be carried out first.

Evidence of tissue stiffening due to collagen fibres, though, prevails in the literature. However, it is the simulation of cross-linking of fibres what replicates the experimentally observed force transmission in the long range. Our results stand in stark contrast in the sense that it was not possible for us to clearly replicate this phenomenon, but only suggest the generation of a directed stiffening, as shown in Figures 4.20 and 4.19. Instead, Ma et al. [45] produced such experimental evidence by culturing fibroblasts in collagen gel, where, as shown in Figure 5.1, the contraction of the cells induces a markedly oriented tension along a chain of collagen fibres. And then, the same authors successfully replicated this observation by creating a finite element model whereby fibres were explicitly discretised and linked together by rigid joints, while embedded in an isotropic matrix, also modelled as an elastic material.

This suggests that our model should incorporate a way to explicitly link together fibres, for their explicit interconnection, rather than just the anisotropy conferred to the hosting matrix, is what underlies the force transmission phenomenon [8, 56, 72], as mentioned in the literature review of the *Introduction* section. In other words, force transmission is preceded by some form of explicit linking between fibres. We mention, however, that the modelling of the fibre at the same scale than the matrix makes reorientation be due solely to the set of prescribed connections among collagen fibres, whereas our implemented model considers the reorientation starting from an initial isotropic condition and evolving due to the state of deformation of the whole material considered as a single continuum.

In spite of this dependence, the results from our tests on the plate with two holes geometry showed that reorientation fades very quickly when moving away from the contracting holes. This is a shortcoming of our model, if we compare these results against those from models that also reorient the fibres by using the deformation state of the surrounding ground substance, for instance, the one presented
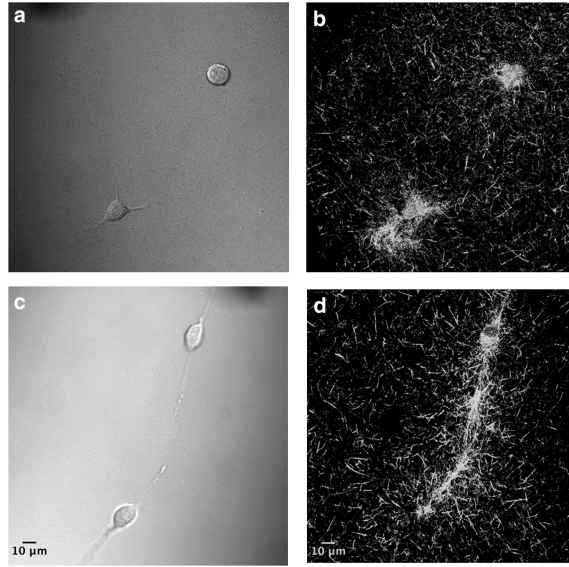
Figure 5.1: Round fibroblasts (a) barely establish a field force around them (b), while, when elongated (c), there is a clear traction path set in between them (d). Image taken from reference [45].

by Wang et al. [74]. We think that our implementation is unable to sufficiently follow that deformation, and that this could stem from, among other causes, the integration scheme applied to the updating of fibre orientations, Equation (3.29).

There, we used a very simplistic forward-Euler expression, while the physical process of biological tissue deformation evolves in a way that suggests application of other, more sophisticated schemes. Therefore, as deformation progresses, the result of our updating formula may lag behind the deformation of the media in which the fibres are embed. The increasingly accumulated error may even introduce spurious results at large strains.

Nevertheless, fibre reorientation was indeed produced by our implementation; its pattern, which would be expected to align almost exclusively in the direction connecting the plate holes, tends to form a varying degree of such reorientation with some kind of lobes symmetric with respect to this direction. This suggests that the eigenvalues of the right-Cauchy Green tensor may have similar magnitudes in the direction of the centre line between the holes and in that perpendicular to it, while the off-diagonal components would be very small in comparison.

The model weaknesses thus discussed must motivate further refinements to our implementation, for even experiments carried out by Rudnicky et al. [61] and a simplified multiscale simulation also presented by the same authors indicate that reorientation of a fibre bundle not only increases the effective stiffness of the host material, but also makes for a propagation of the reorientation of fibres deep into the volume of the ground substance.

In favour of the comparatively small stiffening effect predicted by our model for the plate with two holes, it is suggested that contraction of elongated, rather than round, symmetric cells, makes them exert much larger forces along their longitudinal axis, and so enhances the force transmission action significantly [74]. To this we may further add that the fibre strain energy models used in our work display narrow ranges of stretch over which stresses grow too high, as in the case of the exponential model, or just go beyond some limiting value, as in the case of the WLC model.

In that sense, our simulations failed on the conservative side by applying a value of radial stretch to the holes that was too small. The actual possibility of high gradients of stress on the hole edges must be addressed by first employing a much finer mesh; then, we may think of exploring alternative methods to the classical Newton-Raphson to address the application of load increments in such regions prone to bring about convergence problems; and the use of other hybrid elements apparently less subject to stiffness issues when simulating high stresses.

6

Conclusions

Force transmission in between cells embed in connective tissue is a phenomenon in which many current questions in tissue physiology are matter of research. One factor is that fibre stiffness and orientation plays a significant role in it, as well as the change of the set of orientations under the action of prescribed displacements. These may come from the cells themselves by, for instance, a radial contraction deformation.

In this work we implemented a fibre remodelling formulation to account for the collagen reorientation due to deformation of the isotropic matrix in which these fibres are embed. The model also considers two strain energy functions for the collagen fibres and a Neo-Hookean model for the isotropic ground substance. We used this model to study the force transmission in between cells. To this end, we prepared and ran a UMAT subroutine in Abaqus™ software.

The problem domain is a plate under plane strain with two circular holes in it; each is used to prescribe a radial displacement, so as to replicate cell contraction. We employed performed a set of screening tests over a combination of material and remodelling parameters to identify relevant values of them from the point of view of stiffening and remodelling, and of the propagation of such remodelling away from the boundary of prescribed displacement. To support the study, we also produced a semi-analytic model of the uniaxial tension test and FE simulations of the simple shear test.

While the semi-analytical model revealed marked effects of material and remodelling parameters in the stiffening and in the evolution of anisotropy, the simulation of the plate with two holes case posed an essential difficulty: the material tends to stiffen significantly only at large values of stretching. Once there, stress can grow out of proportion, so that numerical calculations easily fail to converge if the prescribed stretch is close or beyond certain limit. For the same reason, imposing a stretch slightly under such a critical value, intending a fast and unproblematic analysis, makes for a very small stiffening effect.

At these low values of stretch, the stress response is almost completely determined by the stiffness of the ground substance. Only special values of parameters for the fibre stiffness models may make the role of collagen fibre and their reorientation significant. At the other end, the critical stretch values are difficult to assess in complex stress states, just as those taking place close to the hole edges.

The effect of larger stretches under the uniaxial test revealed that, with the exponential model, parameter k_1 controls the stiffening at small stretches, while k_2 is responsible for accumulating the effect at the large ones. In the WLC model, stiffening is more markedly concentrated at these larger stretches. Given that both exponential and WLC are microscale models that use affine deformation, critical values of stretch for the element coincide with those for the micro-scale molecules. This prevents considering interaction among collagen molecules, a phenomenon which is strongly associated to the stiffening effect of the fibres on the tissue.

The remodelling parameter A_Δ poses a limit to the extent of anisotropy gained by each bundle of fibres. However, a high value of it may lead to reorganisation of fibres in more than a single saturation stage. There can be, in fact, conditions where anisotropy reaches its full extent and, at the same time, the material is less stiff than other where anisotropy is not totally developed. These tendencies are virtually the same when using a exponential or a WLC model for the fibre.

As regards the effect of parameter t^*, this depends on the set of properties for the material model of the collagen fibre as well, but its main effect is procuring stiffness to the material; meanwhile, lowering Δt defers the attainment of maximum anisotropy. When the material is kept under the action of prescribed stretch after it has reached its set value, smaller Δ_t, which corresponds to faster application of load, makes the stress at the time this maximum stretch is reached, smaller than that with a larger Δt. However, for smaller Δt the stress value continues growing, although not anymore in an exponential form.

The FE simulation of the uniaxial tension test revealed that fibre reorientation is not uniformly distributed, as stress is, but is greater at the constrained displacement boundaries. However, the remaining set of material parameters may make the stiffening effect of fibre reorientation negligible. Furthermore, for some combination of material properties, the stress calculated by FE was higher than the analytic one, and did not approach it sensibly as the mesh gets finer.

The shear strain FE solution implies a nonuniform stress distribution, with stress localisation on the element edges perpendicular to the shearing plane. On these locations, the stress state is complex, so it is possible to find different degrees of remodelling when going from one edge to the next. However, stress state analysis on the vicinity of the hole edge indicates that the shear contribution to the general stress state is not significant. Whether this scenario still holds as fibre

remodelling evolves must be further investigated.

Finally, even though fibre remodelling was in deed reproduced by our FE implementation, its propagation into the volume of material was less than expected, at least in comparison to experimental observations of the phenomenon and to results from other, not-multiscale modelling attempts. This suggests a further study on three issues: the behaviour of hybrid finite elements applied to a problem where stiffness can grow abruptly; the solution methods, in the sense of exploring alternatives to the usual Newton-Raphson; and the scheme of integration of the evolution equation for fibres, in the sense of using a more sophisticated alternative to the simple forward-Euler used here.

Bibliography

[1] Steven D Abramowitch, Andrew Feola, Zegbeh Jallah, and Pamela A Moalli. Tissue mechanics, animal models, and pelvic organ prolapse: a review. *European Journal of Obstetrics & Gynecology and Reproductive Biology*, 144:S146–S158, 2009.

[2] V Alastrué, MA Martinez, M Doblaré, and Andreas Menzel. Anisotropic micro-sphere-based finite elasticity applied to blood vessel modelling. *Journal of the Mechanics and Physics of Solids*, 57(1):178–203, 2009.

[3] V Alastrué, JF Rodríguez, B Calvo, and M Doblaré. Structural damage models for fibrous biological soft tissues. *International Journal of solids and Structures*, 44(18-19):5894–5911, 2007.

[4] Ellen M Arruda and Mary C Boyce. A three-dimensional constitutive model for the large stretch behavior of rubber elastic materials. *Journal of the Mechanics and Physics of Solids*, 41(2):389–412, 1993.

[5] RM Aspden. Fibre reinforcing by collagen in cartilage and soft connective tissues. *Proceedings of the Royal Society of London. Series B: Biological Sciences*, 258(1352):195–200, 1994.

[6] Ozgur Atalay, Asli Atalay, Joshua Gafford, and Conor Walsh. A highly sensitive capacitive-based soft pressure sensor based on a conductive fabric and a microporous dielectric layer. *Advanced materials technologies*, 3(1):1700237, 2018.

[7] Kendall Atkinson. Numerical integration on the sphere. *The ANZIAM Journal*, 23(3):332–347, 1982.

[8] Allen J Bailey. Molecular mechanisms of ageing in connective tissues. *Mechanisms of ageing and development*, 122(7):735–755, 2001.

[9] Albert J Banes, Greta Lee, Ronald Graff, Carol Otey, Joanne Archambault, Mari Tsuzaki, Michelle Elfervig, and Jie Qi. Mechanical forces and signaling in connective tissue cells: cellular mechanisms of detection, transduction, and responses to mechanical deformation. *Current Opinion in Orthopaedics*, 12(5):389–396, 2001.

[10] P Bažant and BH838076 Oh. Efficient numerical integration on the surface of a sphere. *ZAMM-Journal of Applied Mathematics and Mechanics/Zeitschrift für Angewandte Mathematik und Mechanik*, 66(1):37–49, 1986.

[11] Ted Belytschko, Wing Kam Liu, Brian Moran, and Khalil Elkhodary. *Nonlinear finite elements for continua and structures*. John wiley & sons, 2014.

[12] Ferhun C Caner and Ignacio Carol. Microplane constitutive model and computational framework for blood vessel tissue. *Journal of biomechanical engineering*, 128(3):419–427, 2006.

[13] Alberto Cardona and Michel Géradin. Time integration of the equations of motion in mechanism analysis. *Computers & structures*, 33(3):801–820, 1989.

[14] Jeffrey M Caves, Vivek A Kumar, Adam W Martinez, Jeong Kim, Carrie M Ripberger, Carolyn A Haller, and Elliot L Chaikof. The use of microfiber composites of elastin-like protein matrix reinforced with synthetic collagen in the design of vascular grafts. *Biomaterials*, 31(27):7175–7182, 2010.

[15] MJ Chen, LS Kimpton, JP Whiteley, M Castilho, J Malda, CP Please, SL Waters, and HM Byrne. Multiscale modelling and homogenisation of fibre-reinforced hydrogels for tissue engineering. *European journal of applied mathematics*, 31(1):143–171, 2020.

[16] Ming-Jay Chow and Yanhang Zhang. Changes in the mechanical and biochemical properties of aortic tissue due to cold storage. *Journal of Surgical Research*, 171(2):434–442, 2011.

[17] Mike A Crisfield. *Non-Linear Finite Element Analysis of Solids and Structures*. John Wiley & Sons, 1991.

[18] Min Fang, Jingping Yuan, Chunwei Peng, and Yan Li. Collagen as a double-edged sword in tumor progression. *Tumor Biology*, 35(4):2871–2882, 2014.

[19] Salvatore Federico and Walter Herzog. Towards an analytical model of soft biological tissues. *Journal of biomechanics*, 41(16):3309–3313, 2008.

[20] Behrooz Fereidoonnezhad, C O'connor, and JP McGarry. A new anisotropic soft tissue model for elimination of unphysical auxetic behaviour. *Journal of Biomechanics*, 111:110006, 2020.

[21] Peter Fratzl, Klaus Misof, Ivo Zizak, Gert Rapp, Heinz Amenitsch, and Sigrid Bernstorff. Fibrillar structure and mechanical properties of collagen. *Journal of structural biology*, 122(1-2):119–122, 1998.

[22] YC Fung. Elasticity of soft tissues in simple elongation. *American Journal of Physiology-Legacy Content*, 213(6):1532–1544, 1967.

[23] T Christian Gasser, Ray W Ogden, and Gerhard A Holzapfel. Hyperelastic modelling of arterial layers with distributed collagen fibre orientations. *Journal of the royal society interface*, 3(6):15–35, 2006.

[24] Chiara Giordano and Svein Kleiven. Connecting fractional anisotropy from medical images with mechanical anisotropy of a hyperviscoelastic fibre-reinforced constitutive model for brain tissue. *Journal of the Royal Society Interface*, 11(91):20130914, 2014.

[25] Robert E Guldberg, Christopher S Gemmiti, Yash Kolambkar, and Blaise Porter. Physical stress as a factor in tissue growth and remodeling. *Foundations of Regenerative Medicine: Clinical and Therapeutic Applications*, page 260, 2009.

[26] Albert K Harris, David Stopak, and Patricia Wild. Fibroblast traction as a mechanism for collagen morphogenesis. *Nature*, 290(5803):249–251, 1981.

[27] G Himpel, A Menzel, E Kuhl, and P Steinmann. Time-dependent fibre reorientation of transversely isotropic continua—finite element formulation and consistent linearization. *International journal for numerical methods in engineering*, 73(10):1413–1433, 2008.

[28] Shunji Hirokawa and Hiroki Hasezaki. Model analysis to investigate the contribution of ground substance to ligament stiffening. *Medical engineering & physics*, 32(6):610–616, 2010.

[29] A Gerhard Holzapfel. *Nonlinear Solid Mechanics: A Continuum Approach for Engineering*. Wiley, 2000.

[30] Gerhard A Holzapfel, Thomas C Gasser, and Ray W Ogden. A new constitutive framework for arterial wall mechanics and a comparative study of material models. *Journal of elasticity and the physical science of solids*, 61(1):1–48, 2000.

[31] Gerhard A Holzapfel, Ray W Ogden, and Selda Sherifova. On fibre dispersion modelling of soft biological tissues: a review. *Proceedings of the Royal Society A*, 475(2224):20180736, 2019.

[32] CO Horgan and JG Murphy. A constitutive model for fibre-matrix interaction in fibre-reinforced hyperelastic materials. *Applications in Engineering Science*, 2:100008, 2020.

[33] Thomas JR Hughes. *The finite element method: linear static and dynamic finite element analysis.* Courier Corporation, 2012.

[34] Jay D Humphrey. Continuum biomechanics of soft biological tissues. *Proceedings of the Royal Society of London. Series A: Mathematical, Physical and Engineering Sciences*, 459(2029):3–46, 2003.

[35] Sandra Ilić and Klaus Hackl. Homogenisation of random composites via the multiscale finite-element method. In *PAMM: Proceedings in Applied Mathematics and Mechanics*, volume 4, pages 326–327. Wiley Online Library, 2004.

[36] Brett C Isenberg and Robert T Tranquillo. Long-term cyclic distention enhances the mechanical properties of collagen-based media-equivalents. *Annals of biomedical engineering*, 31(8):937–949, 2003.

[37] RL Jernigan and PJ Flory. Distribution functions for chain molecules. *The Journal of Chemical Physics*, 50(10):4185–4200, 1969.

[38] Jessica WY Jor, Poul MF Nielsen, Martyn P Nash, and Peter J Hunter. Modelling collagen fibre orientation in porcine skin based upon confocal laser scanning microscopy. *Skin Research and Technology*, 17(2):149–159, 2011.

[39] Igor Karšaj, Carlo Sansour, and Jurica Sorić. The modelling of fibre reorientation in soft tissue. *Biomechanics and modeling in mechanobiology*, 8(5):359–370, 2009.

[40] Hanifeh Khayyeri, Anna Gustafsson, Ashley Heuijerjans, Marko K Matikainen, Petro Julkunen, Pernilla Eliasson, Per Aspenberg, and Hanna Isaksson. A fibre-reinforced poroviscoelastic model accurately describes the biomechanical behaviour of the rat achilles tendon. *PloS one*, 10(6):e0126869, 2015.

[41] Hermann Knoche. *Histologie und Histopathologie: Kurzlehrbuch für medizinisch-technische Assistenten.* Springer-Verlag, 2013.

[42] Martin Kroon. An 8-chain model for rubber-like materials accounting for non-affine chain deformations and topological constraints. *Journal of elasticity*, 102(2):99–116, 2011.

[43] GJ Langewouters, KH Wesseling, and WJA Goedhard. The static elastic properties of 45 human thoracic and 20 abdominal aortas in vitro and the parameters of a new model. *Journal of biomechanics*, 17(6):425–435, 1984.

[44] Wen Shing Leong, Chor Yong Tay, Haiyang Yu, Ang Li, Shu Cheng Wu, Duong-Hong Duc, Chwee Teck Lim, and Lay Poh Tan. Thickness sensing of hmscs on collagen gel directs stem cell fate. *Biochemical and biophysical research communications*, 401(2):287–292, 2010.

[45] Xiaoyue Ma, Maureen E Schickel, Mark D Stevenson, Alisha L Sarang-Sieminski, Keith J Gooch, Samir N Ghadiali, and Richard T Hart. Fibers in the extracellular matrix enable long-range stress transmission between cells. *Biophysical journal*, 104(7):1410–1418, 2013.

[46] Huub Maas and Thomas G Sandercock. Force transmission between synergistic skeletal muscles through connective tissue linkages. *Journal of Biomedicine and Biotechnology*, 2010, 2010.

[47] Carmel Majidi. Soft-matter engineering for soft robotics. *Advanced Materials Technologies*, 4(2):1800477, 2019.

[48] Andrew Marantan and L Mahadevan. Mechanics and statistics of the worm-like chain. *American Journal of Physics*, 86(2):86–94, 2018.

[49] A Menzel. A fibre reorientation model for orthotropic multiplicative growth. *Biomechanics and modeling in mechanobiology*, 6(5):303–320, 2007.

[50] Andreas Menzel and Tobias Waffenschmidt. A microsphere-based remodelling formulation for anisotropic biological tissues. *Philosophical Transactions of the Royal Society A: Mathematical, Physical and Engineering Sciences*, 367(1902):3499–3523, 2009.

[51] Jason Mulderrig, Bin Li, and Nikolaos Bouklas. Affine and non-affine microsphere models for chain scission in polydisperse elastomer networks. *Mechanics of Materials*, 160:103857, 2021.

[52] Ramalingam Murugan and Seeram Ramakrishna. Design strategies of tissue engineering scaffolds with controlled fiber orientation. *Tissue engineering*, 13(8):1845–1866, 2007.

[53] David R Nolan, Artur L Gower, Michel Destrade, Ray W Ogden, and JP McGarry. A robust anisotropic hyperelastic formulation for the modelling of soft tissue. *Journal of the mechanical behavior of biomedical materials*, 39:48–60, 2014.

[54] David AD Parry. The molecular fibrillar structure of collagen and its relationship to the mechanical properties of connective tissue. *Biophysical chemistry*, 29(1-2):195–209, 1988.

[55] Christopher J Payne, Isaac Wamala, Colette Abah, Thomas Thalhofer, Mossab Saeed, Daniel Bautista-Salinas, Markus A Horvath, Nikolay V Vasilyev, Ellen T Roche, Frank A Pigula, et al. An implantable extracardiac soft robotic device for the failing heart: mechanical coupling and synchronization. *Soft robotics*, 4(3):241–250, 2017.

[56] Robyn H Pritchard, Yan Yan Shery Huang, and Eugene M Terentjev. Mechanics of biological networks: from the cell cytoskeleton to connective tissue. *Soft matter*, 10(12):1864–1884, 2014.

[57] Peter P Purslow. Strain-induced reorientation of an intramuscular connective tissue network: implications for passive muscle elasticity. *Journal of biomechanics*, 22(1):21–31, 1989.

[58] Peter P Purslow, Tim J Wess, and DW Hukins. Collagen orientation and molecular spacing during creep and stress-relaxation in soft connective tissues. *The Journal of experimental biology*, 201(1):135–142, 1998.

[59] PP Purslow, A Bigi, A Ripamonti, and N Roveri. Collagen fibre reorientation around a crack in biaxially stretched aortic media. *International Journal of Biological Macromolecules*, 6(1):21–25, 1984.

[60] Margot R Roach and Alan C Burton. The reason for the shape of the distensibility curves of arteries. *Canadian journal of biochemistry and physiology*, 35(8):681–690, 1957.

[61] Mathilda S Rudnicki, Heather A Cirka, Maziar Aghvami, Edward A Sander, Qi Wen, and Kristen L Billiar. Nonlinear strain stiffening is not sufficient to explain how far cells can feel on fibrous protein gels. *Biophysical journal*, 105(1):11–20, 2013.

[62] P Sáez, Estefanía Pena, Manuel Doblaré, and MA Martínez. Hierarchical micro-adaptation of biological structures by mechanical stimuli. *International Journal of Solids and Structures*, 50(14-15):2353–2370, 2013.

[63] Ravi K Sawhney and Jonathon Howard. Molecular dissection of the fibroblast-traction machinery. *Cell motility and the cytoskeleton*, 58(3):175–185, 2004.

[64] Josef Arthur Schönherr, Patrick Schneider, and Christian Mittelstedt. Robust hybrid/mixed finite elements for rubber-like materials under severe compression. *Computational Mechanics*, pages 1–22, 2022.

[65] Andreas J Schriefl, Andreas J Reinisch, Sethuraman Sankaran, David M Pierce, and Gerhard A Holzapfel. Quantitative assessment of collagen fibre orientations from two-dimensional images of soft biological tissues. *Journal of The Royal Society Interface*, 9(76):3081–3093, 2012.

[66] David Stopak and Albert K Harris. Connective tissue morphogenesis by fibroblast traction: I. tissue culture observations. *Developmental biology*, 90(2):383–398, 1982.

[67] Andreas Stylianou, Vasiliki Gkretsi, Maria Louca, Lefteris C Zacharia, and Triantafyllos Stylianopoulos. Collagen content and extracellular matrix cause cytoskeletal remodelling in pancreatic fibroblasts. *Journal of the Royal Society Interface*, 16(154):20190226, 2019.

[68] II Tagiltsev and AV Shutov. Geometrically nonlinear modelling of pre-stressed viscoelastic fibre-reinforced composites with application to arteries. *Biomechanics and Modeling in Mechanobiology*, 20(1):323–337, 2021.

[69] Eric A Talman and Derek R Boughner. Glutaraldehyde fixation alters the internal shear properties of porcine aortic heart valve tissue. *The Annals of thoracic surgery*, 60:S369–S373, 1995.

[70] Maliheh Tavoosi, Mehrzad Sharifian, and Mehrdad Sharifian. An efficient exponential based integration for von mises plasticity combined with lemaitre damage model. *Engineering Structures*, 252:113733, 2022.

[71] Peter Thorogood, James Bee, and Klaus von der Mark. Transient expression of collagen type ii at epitheliomesenchymal interfaces during morphogenesis of the cartilaginous neurocranium. *Developmental biology*, 116(2):497–509, 1986.

[72] JA Trotter, J Tipper, G Lyons-Levy, K Chino, AH Heuer, Z Liu, M Mrksich, C Hodneland, W Shannon Dillmore, TJ Koob, et al. Towards a fibrous composite with dynamically controlled stiffness: lessons from echinoderms. *Biochemical Society Transactions*, 28(4):357–362, 2000.

[73] Wolf W von Maltzahn, Rema G Warriyar, and W Ford Keitzer. Experimental measurements of elastic properties of media and adventitia of bovine carotid arteries. *Journal of biomechanics*, 17(11):839–847, 1984.

[74] Hailong Wang, AS Abhilash, Christopher S Chen, Rebecca G Wells, and Vivek B Shenoy. Long-range force transmission in fibrous matrices enabled by tension-driven alignment of fibers. *Biophysical journal*, 107(11):2592–2603, 2014.

[75] Lei Wang, Steven M Roper, XY Luo, and Nicholas A Hill. Modelling of tear propagation and arrest in fibre-reinforced soft tissue subject to internal pressure. *Journal of Engineering Mathematics*, 95(1):249–265, 2015.

[76] Marco PE Wenger, Laurent Bozec, Michael A Horton, and Patrick Mesquida. Mechanical properties of collagen fibrils. *Biophysical journal*, 93(4):1255–1263, 2007.

[77] A Whelan, J Duffy, RT Gaul, D O'Reilly, DR Nolan, P Gunning, C Lally, et al. Collagen fibre orientation and dispersion govern ultimate tensile strength, stiffness and the fatigue performance of bovine pericardium. *Journal of the mechanical behavior of biomedical materials*, 90:54–60, 2019.

[78] Jessamine P Winer, Shaina Oake, and Paul A Janmey. Non-linear elasticity of extracellular matrices enables contractile cells to communicate local position and orientation. *PloS one*, 4(7):e6382, 2009.

[79] E Yamamoto, K Hayashi, and N Yamamoto. Mechanical properties of collagen fascicles from the rabbit patellar tendon. *Journal of biomechanical engineering*, 121(1):124–131, 1999.

[80] Weihao Yuan, Haixing Wang, Chao Fang, Yongkang Yang, Xingyu Xia, Boguang Yang, Yuan Lin, Gang Li, and Liming Bian. Microscopic local stiffening in a supramolecular hydrogel network expedites stem cell mechanosensing in 3d and bone regeneration. *Materials Horizons*, 8(6):1722–1734, 2021.